REPORT DOCUMENTATION PAGE

AFRL-SR-AR-TR-03-

0189

Public reporting burden for this collection of information is estimated to average 1 hour per response, including the time for reviewing instru the data needed, and completing and reviewing this collection of information. Send comments regarding this burden estimate or any other reducing this burden to Washington Headquarters Services, Directorate for Information Operations and Reports, 1215 Jefferson Davis Higl Management and Budget, Paperwork Reduction Project (0704-0188), Washington, DC 20503

1. AGENCY USE ONLY (Leave blank)	2. REPORT DATE	3. REPORT TYPE AND DATES COVERED
	04/14/03	Final, 6/14/99 - 12/14/02

4. TITLE AND SUBTITLE

HIGH PERFORMANCE WOVEN MESH HEAT EXCHANGE

5. FUNDING NUMBERS

F49620 99 1 0286

6. AUTHOR(S)

R.A. Wirtz

7. PERFORMING ORGANIZATION NAME(S) AND ADDRESS(ES)

University of Nevada, Reno
Ross Hall, Rm204/MS325
Reno, NV 89557

8. PERFORMING ORGANIZATION REPORT NUMBER

1330-117-30AG

9. SPONSORING / MONITORING AGENCY NAME(S) AND ADDRESS(ES)

Dr. Thomas Beutner
AFOSR/NA
4015 Wilson Blvd, Rm 713
Arlington, VA 22203-1954

10. SPONSORING / MONITORING AGENCY REPORT NUMBER

11. SUPPLEMENTARY NOTES

12a. DISTRIBUTION / AVAILABILITY STATEMENT

Approved for public release; distribution unlimited.

20030604 061

13. ABSTRACT *(Maximum 200 Words)*

Woven mesh structures, consisting of bonded laminates of plain-weave conductive screens or three-dimensional orthogonal weaves are described. A mathematical model of the thermal performance of such a mesh, deployed as a heat exchange surface shows that the effective conductance of a thin, porous heat exchange matrix is proportional to the square root of the product of the specific surface area, effective thermal conductivity and mesh heat transfer coefficient. Geometric equations show that these porous matrices can be fabricated to have a wide range of porosity and specific surface area. Furthermore, a highly anisotropic thermal conductivity vector can be achieved, with the in-plane effective thermal conductivity ranging to 78.5% of the filament material values.

Measurements of pressure drop and overall heat transfer rate are reported and used to develop correlation equations of mesh friction factor and Colburn j-factor as a function of coolant properties, mesh characteristics and flow rate through the mesh. Experiments with air and water show that mesh heat transfer coefficients and friction factors are comparable to those achieved with other expanded materials. However, high specific surface area coupled with high effective thermal conductivity result in exchange matrices that out-perform other exchange matrix configurations.

14. SUBJECT TERMS			15. NUMBER OF PAGES 56
			16. PRICE CODE
17. SECURITY CLASSIFICATION OF REPORT	18. SECURITY CLASSIFICATION OF THIS PAGE	19. SECURITY CLASSIFICATION OF ABSTRACT	20. LIMITATION OF ABSTRACT
Unclassified	Unclassified	Unclassified	

HIGH PERFORMANCE WOVEN MESH HEAT EXCHANGE

F49620-99-1-0286

Richard A. Wirtz
Mechanical Engineering Department
University of Nevada, Reno
Reno, NV 89557

(775) 784-6714

April 1, 2003

Abstract

Woven mesh structures, consisting of bonded laminates of two-dimensional plain-weave conductive screens, or three-dimensional orthogonal weaves are described. A mathematical model of the thermal performance of such a mesh, deployed as a heat exchange surface, is developed. The model shows that the effective conductance of a thin, porous heat exchange matrix is proportional to the square root of the product of the specific surface area, effective thermal conductivity and mesh heat transfer coefficient. Furthermore, we propose that mesh heat exchange matrices be laid out in a serpentine pattern, similar to the construction of a conventional automotive air filter. This configuration maximizes heat transfer surface area while it minimizes coolant pressure drop (due to the reduced superficial mass velocity). Analysis of a screen-fin heat sink that employs this technology indicates that the optimal convergence/divergence angle of the serpentine layout is $\approx 20° - 30°$.

Geometric equations show that these porous matrices can be fabricated to have a wide range of porosity and specific surface area, with the specific surface area-filament diameter product of 3D stacked weaves approaching 2π. Furthermore, a highly anisotropic thermal conductivity vector can be achieved, with the in-plane effective thermal conductivity ranging to 78.5% of the filament material values.

Measurements of pressure drop and overall heat transfer rate are reported and used with the performance model to develop correlation equations of mesh friction factor and Colburn j-factor as a function of coolant properties, mesh characteristics and flow rate through the mesh. Experiments with air and water show that mesh heat transfer coefficients and friction factors are comparable to those achieved with other expanded materials. However, high β-values, coupled with high effective thermal conductivity result in exchange matrices that out-perform other exchange matrix configurations. This is particularly true for exchange matrix configurations that exploit the higher effective thermal conductivity achievable with this technology.

Contents

Abstract 1

Introduction 4

Heat Exchanger Implementation 5

Thermal Performance Model 6

Plain-Weave Screen Laminates 9

Screen-Laminate Geometry 9

Fabrication Methodology 9

Orthogonal-Weave Porosity, Specific Surface Area and Effective Thermal Conductivity 10

Orthogonal-Weave Heat Transfer and Pressure Drop Correlation 15

Non-orthogonal Weave Porosity, Specific Surface Area, Effective Thermal Conductivity 21

Exchange Matrix Performance Evaluation 24

A P4-Format Heat Sink Based on Screen Laminate Technology 27

Three-Dimensional Orthogonal Weaves 31

Stacked Weave Geometry 31

Mesh Fabrication 31

Porosity, Specific Surface Area and Effective Thermal Conductivity 33

Heat Transfer, Pressure Drop Correlation 37

Exchange Matrix Performance Evaluation 39

Conclusions 42

Research Personnel 44

Research Personnel 44

Publications/Thesis 44

Acknowledgement/Disclaimer 46

References 47

Appendix A: Measurement of *ke* 49

Appendix B: Heat Transfer/Pressure Drop Measurements 52

Introduction

Kays and London [1984] have pointed out that a most effective way to increase the performance of a heat exchanger is to increase its surface area to volume ratio, β. Small-particle packed beds and foamed metals are porous materials having large β-values. Unfortunately, due to the tortuosity effect in conjunction with the high porosity (ε) of these materials, their effective thermal conductivity (ke) is relatively small so that much of the gain in performance obtained by having a large β is lost by having a relatively small ke. Typical values of effective thermal conductivity in fused-particle packed beds are 10% - 15% of the particle thermal conductivity. Commercially available metal foam such as aluminum foam has an effective thermal conductivity that ranges from only 2% to 6% of the base metal value [Calmidi and Mahajan, 1999].

An anisotropic porous matrix having a large specific surface area and a large effective thermal conductivity in a particular direction will result in a very effective heat exchange surface. A woven mesh of heat conducting filaments can be configured to have these characteristics. Geometric equations show that these porous matrices can be fabricated to have a wide range of porosity and specific surface area; and a highly anisotropic thermal conductivity vector can be achieved.

These attributes allow for the design of small, high-performance single-fluid parallel-plate heat exchangers that are more universally applicable than conventional heat exchangers because the mesh can readily be made to conform to complex surface contours. Because of the high thermal conductance achieved, exchangers can be designed for applications where spatial temperature uniformity and/or high localized spot cooling are required.

The present work focuses on two woven mesh configurations:

1. Laminates of plain-weave metallic screens stacked to form a three dimensional structure, and
2. Three-dimensional orthogonal weaves that consist of three metallic wire filaments having their axes aligned with the coordinate axes.

The fabrication methodology for each structure is explored. Models of the porosity, specific surface area, effective thermal conductivity and overall thermal performance of the mesh, deployed as a single-fluid heat exchanger, are developed. Measurements are reported for fabricated test articles; and, mesh Stanton number and friction factor correlations are reported. The thermal performance of the mesh configurations, deployed as heat exchanger surfaces, are evaluated in the light of other surfaces. Prototype heat exchangers are constructed and tested.

Heat Exchanger Implementation

Figure 1 shows a woven mesh implemented as a heat transfer surface in a parallel plate exchanger. The mesh is shown in edge-view in a channel having half-height H. The mesh thickness is t. Heat (q) is conducted from the heated plates (at temperature T_b) into the mesh, and then by convection to the fluid flowing through the mesh. The mesh wire filament axes are arranged with the predominant y-filaments perpendicular to the channel walls so that conduction from the walls is facilitated. Other wire filaments in thermal contact with the predominant filaments act as fins, increasing the specific surface area of the mesh. G_i and $T_{f,i}$ are the coolant approach mass velocity and temperature, respectively. ΔP is the pressure drop across the exchange matrix. The right-hand segment of the figure shows the expected temperature distribution of the woven mesh (T_s) and the exit-plane coolant ($T_{f,o}$).

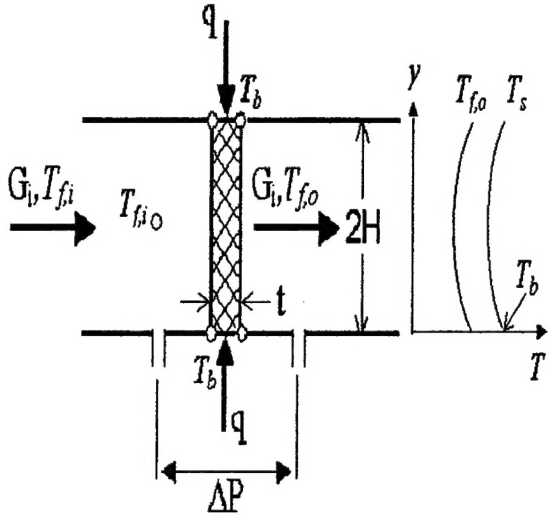

Fig. 1 Heat exchange implementation of a thermally conductive woven mesh.

Figure 2 shows a plan view of a segment of the coolant passage of a plate-fin heat exchanger. Fin stock normally found between the plates is replaced with a woven-mesh porous wall that is laid out in a serpentine pattern. Mesh wire filaments are oriented between the side plates of the exchanger as in Fig. 1. The woven-mesh porous wall segment so formed is shown in plan view, and typical flow paths for some fluid elements are shown. This configuration results in a relatively low coolant pressure drop since fluid parcel paths through the mesh are short, and the serpentine mesh layout results in a large face area leading to low superficial mass velocities of coolant through the mesh. The divergence/convergence angle of wall segments, 2ϕ controls the flow

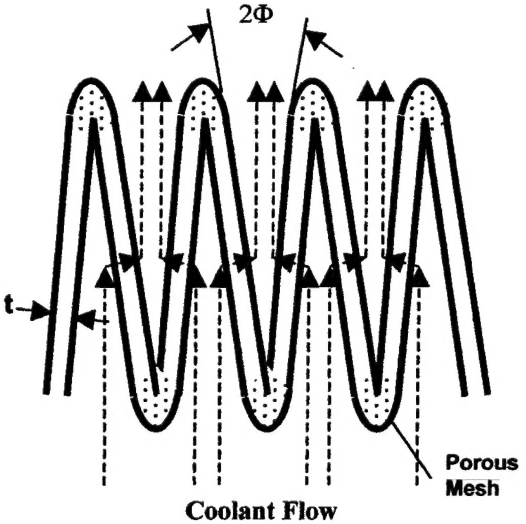

Fig. 2 Plan view of woven mesh serpentine wall. Divergence angle controls uniformity of flow through wall segments.

uniformity through each segment. Heat transfer is by conduction through the module side plates, and then by conduction and convection within the (porous) woven mesh.

Thermal Performance Model

The mesh acts as a porous wall of porosity, ε and thickness, t. The heat transfer rate is given by

$$q = U(tW)\left[T_b - T_{f,i}\right] \tag{1}$$

where U is the effective conductance of the porous wall and (tW) is the porous wall base area.

The porous wall effective conductance, U can be related to the thermal and physical characteristics of the woven structure. The fluid flow path length through the porous wall is short and flow rates are relatively high, so local thermal equilibrium between the fluid and solid phases is probably not achieved; a two energy equation model is called for. Wirtz [1997] assumes that the solid phase temperature is only a function of y, and the local heat flux between the fluid and solid phases is characterized by Newton's cooling law

$$q'' = h\left[T_s(y) - T_f(x,y)\right] \tag{2}$$

where h is the mesh heat transfer coefficient. Eq. (*2*) couples the solid and fluid phase energy equations.

An energy balance on a dy· t slice of solid phase material, which balances the increase in internal energy of the fluid phase with the net conduction in the solid phase, leads to the following solid-phase energy equation

$$\frac{d^2T_s}{dy^2} = \frac{cG_i}{ke_y t}\left[T_{f,o}(y) - T_{f,i}\right] \tag{3}$$

with boundary conditions: $T_s(0) = T_b$ and $\left.\frac{dT_s}{dy}\right|_{y=H} = 0$ (symmetrical heating assumed). An energy balance on a dx· dy element of fluid, which introduces the particle heat transfer coefficient through eq. (*2*), gives

$$\frac{\partial\tau}{\partial x} + \frac{\beta St}{\varepsilon}\tau = 0 \tag{4}$$

where $\tau = T_s(y) - T_f(x,y)$, with boundary condition $\tau(0,y) = T_s(y) - T_{f,i}$. $St = \frac{\varepsilon h}{cG_i}$ is the mesh Stanton number. Wirtz [1997] assumes that $T_f(x,y) = (T_{f,i} + T_{f,o})/2$. This assumption leads

to closure of the two energy equations. The following is an extension of the above-described model, which does not make this assumption.

Assume the porous wall has uniform porosity and thickness. Then, the fluid flowing through the porous wall will follow parallel streamlines (y = constant) so that a parcel of fluid will be exposed to solid phase material at a fixed temperature. Further assume that h = constant. Then eq. (*4*) can be integrated across the porous wall to give

$$T_{f,o}(y) - T_{f,i} = \left[T_s(y) - T_{f,i}\right]\left(1 - e^{-ntu}\right) \tag{5}$$

with $ntu = St \cdot \frac{\beta \cdot t}{\varepsilon}$ the number of transfer units of the mesh. Substitution of eq. (*5*) into eq. (*3*) and integration gives the solution for the solid phase temperature distribution

$$\frac{T_s(y) - T_{f,i}}{T_b - T_{f,i}} = \frac{\cosh\left[m(H-y)\right]}{\cosh\left[mH\right]} \tag{6}$$

$$mH = \sqrt{\hat{G}_i\left(1 - e^{-ntu}\right)} \tag{7}$$

where $\hat{G}_i = \frac{cG_iH^2}{ke_yt}$ is a dimensionless coolant superficial mass velocity. Then, the heat flux $q_b'' = -ke_y \left.\frac{dT_s}{dy}\right|_{y=0}$ may be determined by differentiating eq. (*6*). Substitution of the result into eq. (*1*) gives

$$\frac{UH}{ke_y} = mH \cdot \tanh(mH) \tag{8}$$

Finally, recognizing that the maximum heat transfer rate occurs when all the coolant is heated to the base temperature of the porous wall, we can write an expression for the effectiveness of the screen laminate fin

$$\eta \equiv \frac{q_b''}{q_b''(\max)} = \sqrt{\frac{1 - e^{-ntu}}{\hat{G}_i}} \tanh(mH) \tag{9}$$

Figure 3 compares the effectiveness of the present model, eq. (9) with that of Wirtz [1997]. The figure plots the exchange matrix effectiveness versus number of transfer units for two dimensionless superficial mass velocities. The figure shows that the new model gives a smooth

variation in effectiveness as a function of ntu, and it predicts η somewhat lower than the previous model. The effectiveness is seen to asymptote to unity as ntu increases when $\hat{G}_i \to 0$.

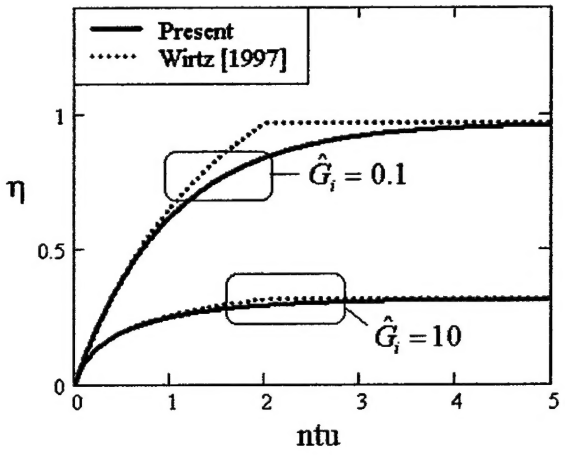

Fig. 3 Comparison of porous models.

Equations (7) and (8) show that

$$U \approx \sqrt{\beta k e_y h} \cdot F(ntu) \qquad (10)$$

where, for the current application, $F(ntu) \approx O(1)$. Therefore, thermal performance is maximized by increasing the specific surface area (β), the effective thermal conductivity (ke_y), and the mesh heat transfer coefficient (h).

Plain-Weave Screen Laminates

Screen-Laminate Geometry

Figure 4 shows two-dimensional plain-weave screens stacked together to form a screen laminate. Each screen has woven wires of diameter *dy* and *dz*, with axis parallel to the *y-* and *z-axis*, respectively. Wire spacing is designated by the mesh numbers, *My* and *Mz*. The laminate has thickness, $t = cf \cdot n(dy + dz)$, where *n* is the number of screen layers of the lamination, and *cf* is the compression factor. *cf* accounts for interleaving of wire filaments of adjacent screens, and wire crimping at wire intersections. Wire filaments are bonded at intersections to facilitate conduction; and, successive screen layers are bonded together to add rigidity to the structure. Successive screens can be arranged "*in-line*" as shown in Figure 4, or in "*staggered*" configuration, where alternate screen layers are offset in the *y* and *z* directions by 0.5 M^{-1}. Screen laminates having *dy* = *dz* and *My* = *Mz* are designated isotropic. If the angle between wire filament axes (the weave angle) is 90°, as shown in Fig. 4, the screen is an orthogonal weave. Non-orthogonal weaves (diamond weaves) are also possible.

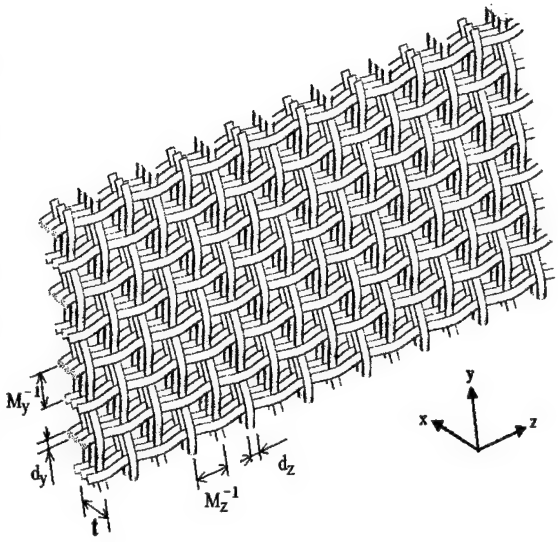

Fig. 4 Screen laminate geometry.

Fabrication Methodology

Screen laminate fabrication is very straightforward. Commercial grade screen is stacked to form a lamination with the screen elements either aligned or staggered. The wire filaments are then dip-brazed or re-flow soldered to bond the wire filaments at their intersections, and bond adjacent screens together. The resulting structure is very stiff. In fact, there is a commercial stainless steel filter product called Rigimesh®.

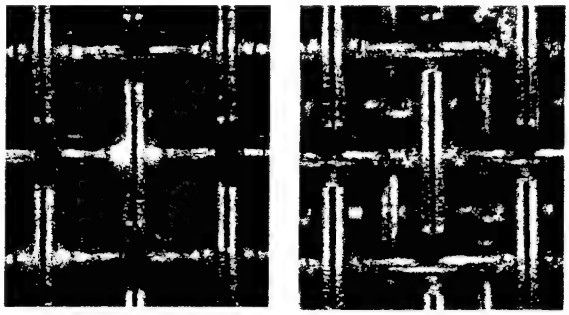

Fig. 5 Inline and staggered plain-weave screen laminates.

Figure 5 shows multi-ply prototypes with *d* = 0.432 mm (0.017"), *M* = 20 in^{-1}. The two different screen alignments are shown: the in-

line configuration has successive screens with wire filaments aligned, and the staggered configuration has screens stacked somewhat randomly, while wire filaments are aligned with the y-and z-axis. Commercial grade copper screen (k_s = 400 W/mK) is pre-coated with a solder bearing flux (95% Sn/5% Pb, k_s = 55-60W/mK). Screen layers are stacked in a fixture, and the assembly is re-flow soldered at 230°C. The inline configuration has $\varepsilon = 0.7$, $\beta = 2700$ m^{-1}, and ke_y = 50 W/mK. The staggered configuration has $\varepsilon = 0.63$, $\beta = 3350$ m^{-1}, and ke_y = 62 W/mK.

Orthogonal-Weave Porosity, Specific Surface Area and Effective Thermal Conductivity

Figure 6 shows plan and edge views of a section of screen. Serpentine wire filaments have diameter dx and dy, and corresponding mesh numbers Mx and My. The wire filament pitch in the x- and y-directions are Mx^{-1} and My^{-1}, respectively. In the absence of crimping, a single screen has thickness $t_1 = dx + dy$. Filament lengths are, [Luo and Mitra, 1999]

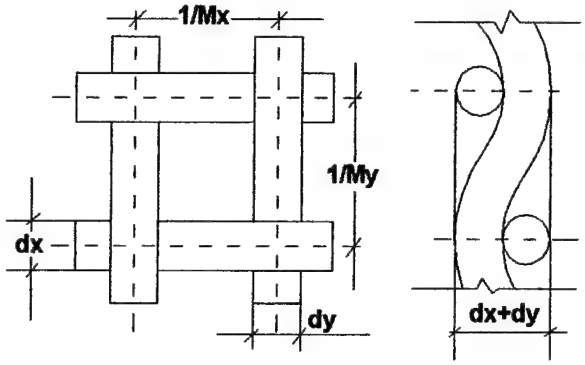

Fig.6 Orthogonal weave unit cell

$$Sx = \frac{1}{Mx}\left[1 + 9.6\left(\frac{dy \cdot Mx}{4}\right)^2 - 49.2\left(\frac{dy \cdot Mx}{4}\right)^4\right] \tag{11}$$

$$Sy = \frac{1}{My}\left[1 + 9.6\left(\frac{dx \cdot My}{4}\right)^2 - 49.2\left(\frac{dx \cdot My}{4}\right)^4\right] \tag{12}$$

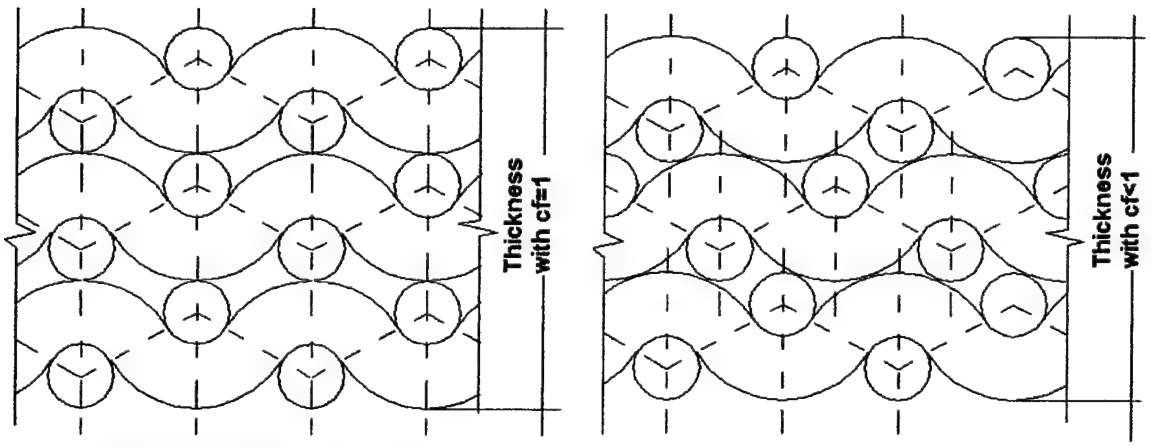

Fig. 7 Screen stacking configurations.

Figure 7 shows two possible arrangements of stacked plain-weave screens. The leftr view shows the situation where successive wire filaments are aligned so that the thickness of a laminate

consisting of n screens is $t_n = n(dx + dy)$. The right view shows the situation where successive wire filaments are not necessarily in line so there is some interleaving of wire filaments when the screens are stacked. In this case, the thickness of the laminate is $t_n = n \cdot c_f (dx + dy)$ where c_f is the compression factor. The magnitude of the compression factor depends on the weave pattern, mesh numbers and wire filament diameters of the screen, and the stacking arrangement of the screen layers. If we restrict our attention to screens with $t_1 = dx + dy$, then $cf \leq 1$.

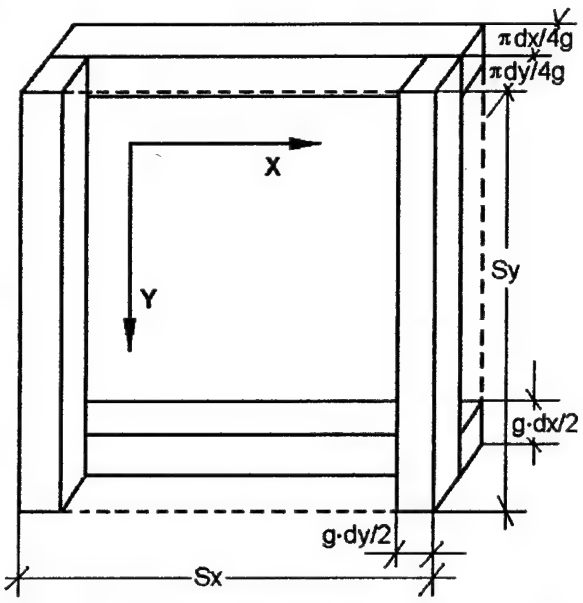

Fig. 8 Orthogonal weave transformed unit cell.

Consideration of Figs. 6 and 7 leads to expressions for the porosity, ε and specific surface area, β of orthogonal plain-weave screen laminates.

$$cf \cdot (1 - \varepsilon) = \frac{\left(\pi \cdot dy^2 Sy + \pi \cdot dx^2 Sx\right) \cdot Mx \cdot My}{4(dx + dy)} \tag{13}$$

where $cf(1 - \varepsilon)$ is the "reduced" metal fraction.

$$\beta = SF \cdot (1 - \varepsilon) \tag{14}$$

SF in Eq. (4) is the shape factor for the particular weave pattern and stacking arrangement

$$SF = \frac{4(dy \cdot Sy \cdot Mx + dx \cdot Sx \cdot My)}{dy^2 \cdot Sy \cdot Mx + dx^2 \cdot Sx \cdot My} \tag{15}$$

If we introduce the mesh number and wire filament diameter ratios $\overline{M} = My / Mx$ and $\overline{d} = dx / dy$, then it can be shown [Xu, 2001] that the reduced metal fraction is a function of $(Mxdy, \overline{M}, \overline{d})$ and β is a function of $((1 - \varepsilon), cf, \overline{M}, \overline{d})$.

Koh and Fortini [1973] and Chang [1990] have reported models and empirical correlations specifically directed at the cross-plane effective thermal conductivity component of screen material. We have found no reference in the technical literature for the in-plane component of the effective thermal conductivity.

Following Chang [1990], we transform the segment of screen unit cell shown in Fig. 6 to the layered, rectangular cross section segment shown in the figure 8. Each rectangular wire filament has thickness $\pi d / 4g$ and width gd so that the cross section area of each filament is $\pi d^2 / 4$. The geometric index, g is a measure of the contact between wire filaments at intersections.

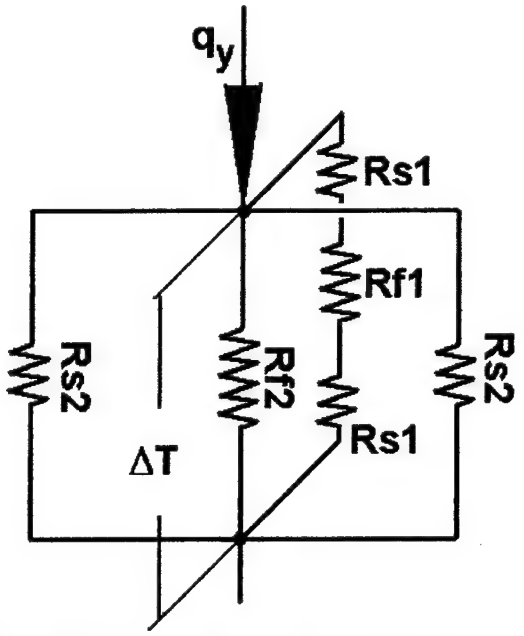

Fig. 9 Orthogonal weave thermal circuit.

The in-plane effective thermal conductivity in the y-direction may be determined by considering the thermal circuit for conduction across the transformed unit cell, shown in Fig. 9. The figure shows three heat-flow paths: R_{s2} is the thermal resistance for conduction along the axis of the y-wire filaments; R_{s1} is the thermal resistance across x-wire filaments; R_{f1} is the thermal resistance to conduction in the y-direction across the intervening "fluid" lying between x-wire filaments; and, R_{f2} is the thermal resistance of the fluid slab that lays between the y-wire filaments. These resistances are given as

$$R_{s1} = \frac{2g^2 \cdot dx}{\pi \cdot Ks \cdot dx \cdot Sx} \tag{16}$$

$$R_{s2} = \frac{8Sy}{\pi \cdot K_s \cdot dy^2} \tag{17}$$

$$R_{f1} = \frac{4g \cdot Sy(My, dx) - 4g^2 dx}{\pi \cdot K_f \cdot dx \cdot Sx} \tag{18}$$

$$R_{f2} = \frac{4g \cdot Sy}{\pi \cdot K_f \cdot (Sx - g \cdot dy) \cdot dy} \tag{19}$$

We further require that the volume of wire filaments be preserved across the geometric transformation shown in Fig. 8. Then $g = \pi / (4 \cdot cf)$. The Y-direction conductance across the transformed unit cell is,

$$R_{tot}^{-1} = ke_y \frac{cf \cdot Sx \cdot (dx + dy)}{Sy} \tag{20}$$

where R_{tot} is the overall thermal resistance of the thermal circuit (Fig. 9) and ke_y is the Y-direction in-plane effective thermal conductivity of the screen. Rearranging Eq. (20) gives

$$cf \cdot \overline{K}_{ey} = \frac{160\pi \cdot Mxdy \cdot (\overline{K}_{fs} - 1) + C \cdot cf \cdot \overline{K}_{fs}}{(\overline{d}+1) \cdot D} + \frac{C \cdot cf^2 \cdot \overline{d} \cdot \overline{K}_{fs}}{(\overline{d}+1) \cdot (160\pi \cdot \overline{d} \cdot \overline{M} \cdot cf \cdot Mxdy(1 - \overline{K}_{fs}) + C \cdot cf)} \quad (21)$$

where

$$C = 123(Mx \cdot dy)^4 - 384(Mx \cdot dy)^2 - 640 \quad (22)$$

$$D = 123(My \cdot dx)^4 - 384(My \cdot dx)^2 - 640 \quad (23)$$

and $\overline{Ke}_y = ke_y / k_s$, $\overline{K}_{fs} = k_f / k_s$ are the dimensionless effective conductivity and "fluid" conductivity, respectively.

Isotropic Laminates Since most available commercial woven mesh products are isotropic structures, i.e *dx=dy=d and Mx=My=M,* the above general results can be simplified to the following:

$$cf[1 - \varepsilon(iso)] = -3.906 \times 10^{-4} \pi \cdot C \cdot Md \quad (24)$$

$$\beta(iso) = 4(1 - \varepsilon)/d \quad (25)$$

$$cf \cdot \overline{K}_e(iso) = \frac{80\pi \cdot Md \cdot (\overline{K}_{fs} - 1) + C \cdot cf \cdot \overline{K}_{fs}}{C} + \frac{C \cdot cf^2 \cdot \overline{K}_{fs}}{320\pi \cdot Md(1 - \overline{K}_{fs}) + 2C \cdot cf} \quad (26)$$

Equation 24 shows that the reduced "metal fraction" of isotropic screen laminates, $cf(1-\varepsilon)$ is solely a function of the *Md*-product of the mesh. We note that $Md \to 1$ designates a "tightly" woven screen. In actuality, there is a physical limit on the magnitude of *Md*. For isotropic plain-weave screens where the thickness is limited to t_l=*2d*, $Md(\max) = 1/\sqrt{3} = 0.577$ so that the porosity is limited such that $0 < cf(1-\varepsilon) < 0.534$.

Equation 25 shows that the specific surface area, β of isotropic structure follows the functional form of other porous media, with *SF = 4/d*. By contrast, *SF(spheres) = 6/d*$_s$ for an unconsolidated bed of spherical particles. Finally, Equation 26 shows that the effective conductivity $\overline{Ke}_y(iso)$ is solely a function of *cf*, $\overline{K}_{fs}$ and *Md*.

Discussion Figure 10 plots the reduced metal fraction as a function of *Mxdy*. The case for an isotropic screen laminate is shown as a solid line. This case always produces screen laminates

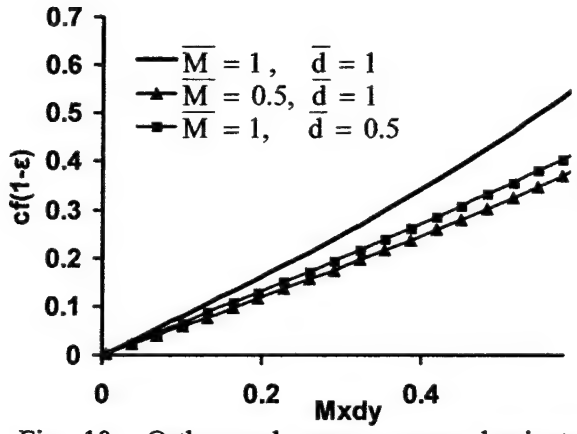

Fig. 10 Orthogonal weave screen laminate reduced metal fraction.

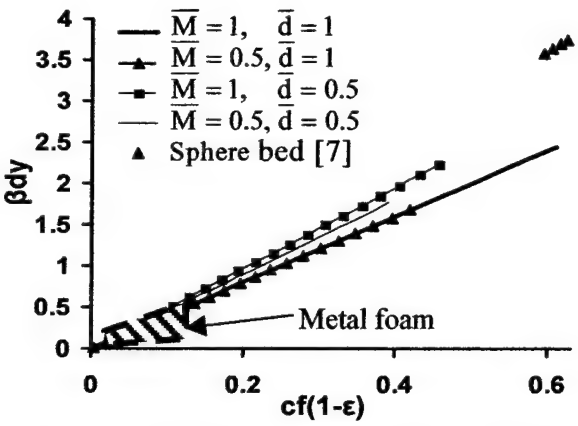

Fig. 11 Orthogonal weave screen laminate specific surface area.

having the highest reduced metal fraction (lowest porosity). The reduced metal fraction for two anisotropic plain-weave laminate cases ($\overline{M} < 1$, $\overline{d} < 1$) are also shown in the figure.

Figure 11 plots βdy as a function of reduced metal fraction. The case for an isotropic screen laminate is shown as a bold solid line. The shape factor for this condition is SF = 4 (the slope of the plotted line). This is true for all conditions where $\overline{d} = 1$. The case $\overline{M} = 0.5$, $\overline{d} = 1$ is shown superimposed on the isotropic case. All conditions with $\overline{M} < 1$, $\overline{d} < 1$ lead to larger values of βdy at fixed $Mxdy$. Therefore, the condition $\overline{d} = 1$ always produces the smallest specific surface area.

Figure 11 compares βd_y of screen laminates with a bed of fused spheres and metal foams. The theoretical porosity of a packed bed of unconsolidated spheres depends on the packing arrangement [Kaviany, 1995]. It can range from $\varepsilon = 0.26$ for face centered cubic packing to $\varepsilon = 0.476$ for simple cubic. However, the *achievable* porosity of a packed bed is difficult to control. A typical porosity for an unconsolidated bed will range from 0.37 to 0.41. As a consequence, the metal fraction can range from 0.59 to 0.63 and βd will then range from 3.54 to 3.78. The range of the specific surface area achievable with uncompressed metallic foams [Ashby et al, 2000] is also displayed. Depending on the origin of the data for foams, screen laminates provide either a significant increase in specific surface area, or they are comparable to the foams. In any case, screen laminates extend the range of metal fraction (or porosity) beyond what appears to be achievable with metal foam.

Figure 12 plots the reduced effective conductivity as a function of reduced metal fraction. The case for an isotropic screen laminate with $\overline{K}_{fs} = 0$ is shown as a bold solid line. An additional case, isotropic screen laminate with $\overline{K}_{fs} = 0.1$ is also shown (solid line). Under these conditions,

the effective conductivity is shifted upward approximately proportional to the value of $\overline{K}_{fs}$. In many applications where the second phase material is a hydrocarbon with the first phase a "good" conductor, $\overline{K}_{fs} < 0.005$. Two additional, anisotropic screen laminate cases are shown in the figure. Cases with $\overline{M} < 1$ or $\overline{d} < 1$ always produce effective conductivities that are greater than obtained with isotropic plain-weaves.

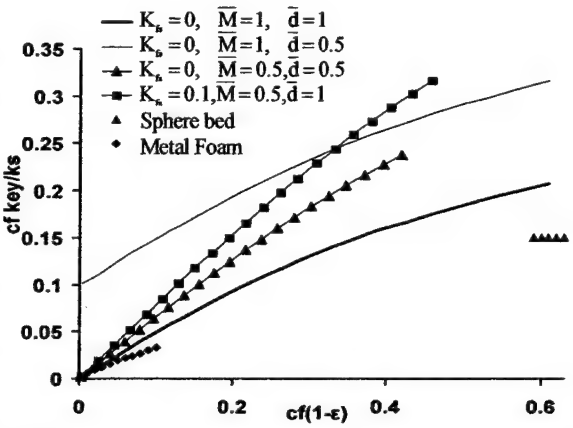

Fig. 12 Orthogonal weave screen laminate conductivity.

It is easy to find the maximum possible value of $\overline{Key}$. When $Mxdy \to 1$, $\overline{M} \to 0$ and $\overline{d} \to 0$, then, Eq. (21) gives,

$$Ke_y(\max) = \frac{(1-\pi)k_{fs}}{4} + \frac{\pi}{4} \qquad (27).$$

The dimensionless effective thermal conductivity of anisotropic screen laminate structures could be easily configured with a value of more than 0.3, with the reduced metal fraction of about 0.4. Comparing with a fused bed of spheres, which are expected to have Ke_y(spheres) ≈ 0.15 with metal fraction, 1-ε ≈ 0.6, this represents an approximate two-fold increase in thermal performance relative to fused sphere heat transfer matrices. The value ranges of effective conductivity and metal fraction of the metal foam [Calmidi and Mahajian, 1999] are also shown in the figure. By virtue of their higher effective thermal conductivity, the screen laminates structures offer a two- to four-fold improvement in performance relative to high-porosity exchange matrices fabricated from metallic foam.

Model Verification. Transient thermal diffusivity measurements of screen laminate samples (Appendix A) shows that the prediction of the present model is within 10% of all of the measurements.

Orthogonal-Weave Heat Transfer and Pressure Drop Correlation

Tong and London [1957] reported measurements of friction factor and mesh heat transfer coefficient for inline plain weave laminates and staggered cross-rod matrices (no interweaving). They used a calorimetric method to measure the local heat transfer coefficient of one heated filament inside the array. Since other filaments upstream of the "measurement filament" were not heated, their correlations are expected to predict heat transfer coefficients that are higher than

would be expected if all wire filaments of the array were heated. Miyabe et al. [1982] report heat transfer coefficient correlations for plain-weave screen laminates that are in close agreement with those of Tong and London. However, they do not describe their measurement techniques. Armour and Cannon [1968] report pressure drop correlations for plain-weave screens, but not laminations of screens.

We postulate that the pressure drop across the mesh, ΔP, is functionally related to fluid flow properties and divergence angle Φ (Fig. 2) as follows:

$$\frac{\Delta P}{t} = fn(\rho, G, \mu, d, \beta, \varepsilon, \Phi) \tag{28}$$

where $G = \frac{G_i}{\varepsilon}$ is the internal mass velocity. Then dimensional analysis gives

$$f = fn(\mathrm{Re}, \varepsilon, \Phi) \tag{29}$$

where $f = \frac{2\rho\Delta P}{G^2 \beta t}$ is the friction factor, and $\mathrm{Re} = \frac{GD_h}{\mu}$ is the mesh Reynolds number, with $D_h = \frac{4\varepsilon}{\beta} = \frac{\varepsilon d}{1-\varepsilon}$ the mesh hydraulic diameter.

In a similar way, we postulate that the mesh heat transfer coefficient, h is functionally related to fluid and flow properties as follows:

$$h = f(\rho, G, \mu, d, \beta, t, \varepsilon, \mathrm{Pr}, \Phi) \tag{30}$$

Dimensional analysis gives

$$St = fn(\mathrm{Re}, \mathrm{Pr}, d/t, \varepsilon, \Phi) \tag{31}$$

where Pr is the Prandtl number of the coolant. In the following, we describe experiments to determine the specific form of eqs. (29) and (31).

Heat Transfer and Pressure-Drop Correlations, Orthogonal Flow Experiments are performed to measure the pressure drop and porous wall effective conductance for isotropic screen laminates with the approach flow normal to the screen lamination (Φ = 90°). Then, the mesh Stanton number is determined from eq. (8). The friction factor and Stanton number correlations are found in the case of inline and staggered configuration respectively. The test faciloity and experimental procedures are described in Appendix B.

Figure 13 summarizes pressure drop measurements for inline and staggered screen-laminates. The staggered screen-laminate friction factor is much higher than the friction factor of the inline configuration. The present data for the inline correlation is correlated with the following expression

$$f = \left(0.39 + \frac{24.5}{\mathrm{Re}}\right)\left(\frac{\varepsilon}{1-\varepsilon}\right)^{0.4} \quad (32)$$

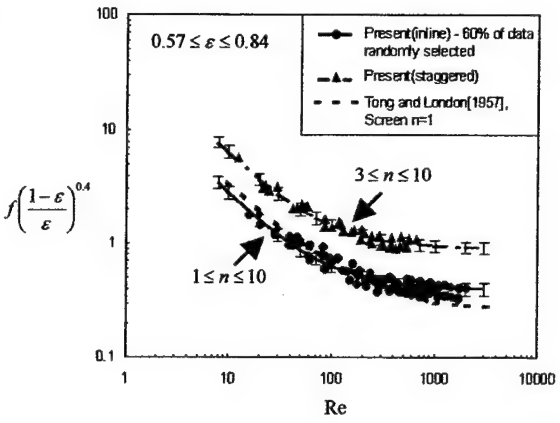

Fig. 13 Friction factor of inline and staggered stacked screen laminates

The expression contains an inertial loss term and a viscous term. We note that $\frac{\varepsilon}{1-\varepsilon} = \frac{D_h}{d}$. These results are compared with Tong and London's data. The present screen laminates are bonded whereas those of Tong and London are not; bonding fillets at wire intersections probably gives rise to higher inertial losses at high Reynolds numbers. Eq. (32) reproduces the data that generated it with a standard error of ±20%.

Figure 13 also shows the friction factor vs. Reynolds number correlation for staggered screen laminate stacking. In this case, the data is correlated as follows

$$f = \left(0.9 + \frac{55.3}{\mathrm{Re}}\right)\left(\frac{\varepsilon}{1-\varepsilon}\right)^{0.4} \quad (33)$$

The data show that staggered stacking results in an approximate two-fold higher pressure loss than inline stacking at the same flow rate. Eq. (33) reproduces the data that generated it with a standard error of ±15%.

Heat transfer experiments are performed with chilled water (Pr ≈ 9.5). We are correlating data in terms of Colburn j-factor so that a direct comparison can be made with the data reported by Tong and London, who experimented with air (Pr = 0.7). We have chosen to correlate the data with a power-law. A regression analysis yielded the following results.

$$j = St \cdot \mathrm{Pr}^{\frac{2}{3}} = 5.86\,\mathrm{Re}^{-0.68}\left(\frac{\varepsilon}{1-\varepsilon}\right)^{-0.2}\left(\frac{d}{t}\right) \quad \text{(in-line)} \quad (34)$$

$$j = St \cdot \mathrm{Pr}^{\frac{2}{3}} = 2.63\,\mathrm{Re}^{-0.65}\left(\frac{\varepsilon}{1-\varepsilon}\right)^{-0.2}\left(\frac{d}{t}\right) \quad \text{(staggered)} \quad (35)$$

Figure 14 summarizes heat transfer data (both inline and staggered configurations) in terms of modified j-factor as a function of Reynolds number. The modified j-factor correlation for the inline correlation is plotted as continuous line and compared with Tong and London's correlation for air. Tong and London's data are adjusted to conform to the definition in the present case and then plotted as a dashed line. Comparing the present correlation with the Tong and London's data, the magnitude of the present data is smaller than the correlations of Tong and London at the higher Reynolds number. Otherwise, the results are in close agreement. This implies that the present correlation is applicable to coolants with 0.7<Pr<9.5. The figure also shows that the staggered configuration produces a lower modified j-factor than does the inline configuration. This is a somewhat surprising result. Eqs. (34, 35) reproduce the data that generated them with a standard error of ±18%.

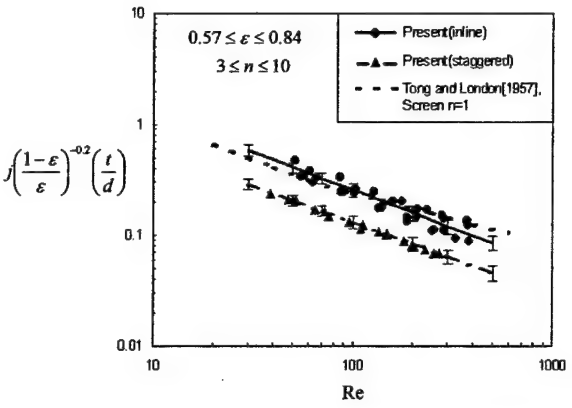

Fig. 14 Modified Colburn j-factor of inline and

Heat Transfer and Pressure-Drop Correlations, Non-Orthogonal Flow Both pressure drop and heat transfer are measured for a single layer of isotropic screen with air as described in Appendix B. Test articles with different divergence angles ($6° \le 2\varphi \le 180°$) and laminate heights (16.1mm $\le$ H $\le$ 28.4mm) are investigated. All of our test articles are made of solder-bonded copper screen with d = 0.48 mm (0.019"), M = 7.9 cm^{-1} (20in^{-1}) with $\varepsilon = 0.677$, $\beta = 2.68\times10^{3} m^{-1}$, and $key = 55.2\frac{watt}{m\cdot K}$ as estimated by Eq. (24 – 26)

In Fig. 15, we present just several sets of pressure drop data (φ =3°, 7.1°, 20°, 34°, 90°) in terms of modified friction factor, $F = f\cdot\left(\frac{1-\varepsilon}{\varepsilon}\right)^{0.4}$. The data is best correlated with the following expression:

$$F = \left(0.39 + \frac{24.5}{\mathrm{Re}}\right) + \left(\frac{0.17}{\tan(\varphi)^2} + \frac{26.3}{\mathrm{Re}^{1.16}\tan(\varphi)}\right) \qquad (36)$$

The expression contains both inertial loss terms and viscous terms. The first two terms are for φ =90° (Eq. 32), and the second two terms reflect the effect of variations in screen-fin divergence angle. Eq. (36) reproduces the data that generated it with a standard error less than ±10%.

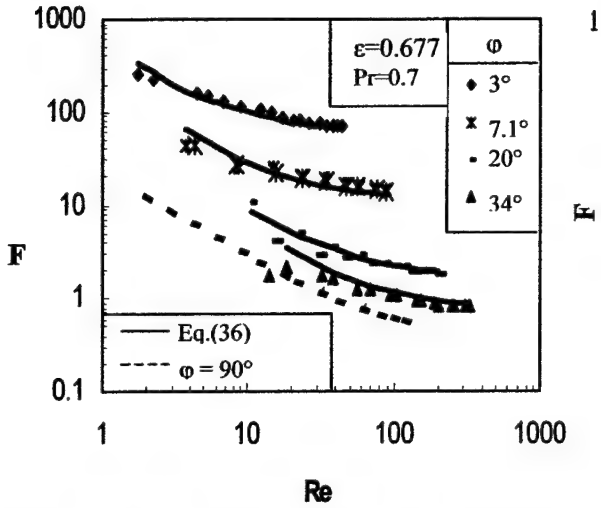

Fig. 15 Modified friction factor non-orthogonal flow.

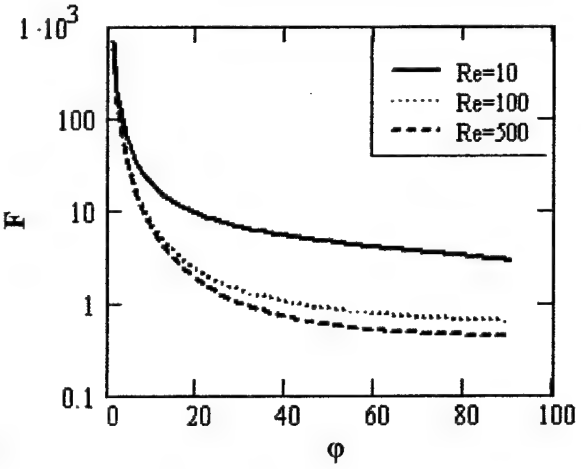

Fig. 16 F factor versus divergence angle

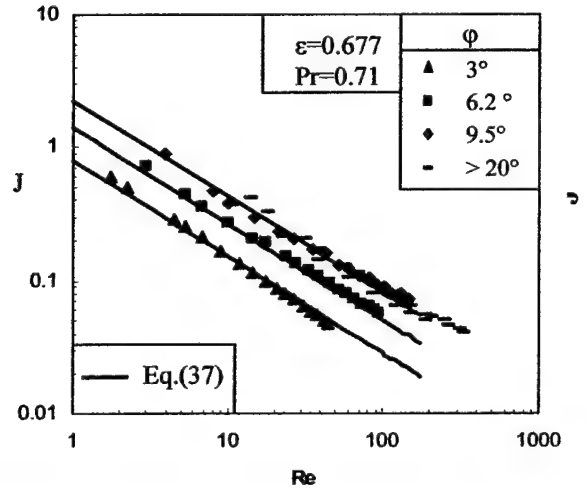

Fig. 17. J Factor of Screen Laminate Heat Sink

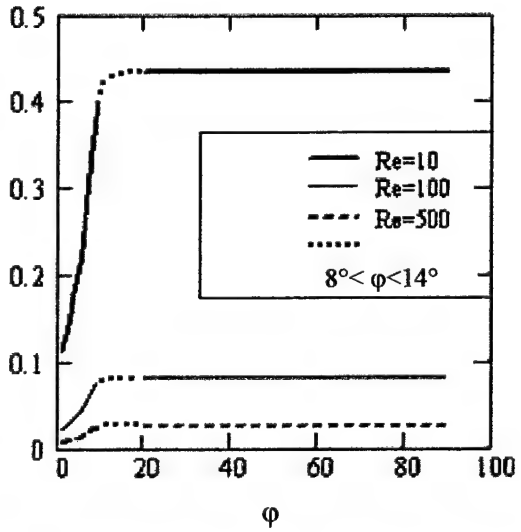

Fig. 18. Non-orthogonal flow modified J Factor versus φ, Eq. (37)

Figure 16 plots the modified friction factor, Eq.(36) as a function of φ for three Reynolds numbers. As shown in the figure, F decreases very sharply when $0 < \theta < 20°$ and the curve becomes flat when the θ is greater than about 40°.

Figure 17 summarizes heat transfer data in terms of modified Colburn j-factor, $J = j \cdot \left(\frac{1-\varepsilon}{\varepsilon}\right)\left(\frac{t}{d}\right)$ as a function of Reynolds number. Data for φ = 3°, 6.2°, 9.5° and φ ≥ 20° are plotted. The figure shows that J is sensitive to φ when it's less than about 14°; and, variations in θ have no significant effect on J when θ is greater than 14°. We have chosen to correlate the

data with a power-law. A regression analysis yielded the following results. Eq. (37) reproduces the data that generated it with a standard error of ±7 %.

$$J = \begin{cases} A(\varphi)\,\mathrm{Re}^{-.72} & 0^o \le \varphi \le 8^o \\ 4.6\left[A(\varphi - 4.3^o)\right]^{0.9} - 2.72\left[A(\varphi - 4.3^o)\right]^{1.2}\,\mathrm{Re}^{-0.72} & 8^o < \varphi < 14^o \\ 2.36\,\mathrm{Re}^{-0.72} & 14^o \le \varphi \end{cases} \tag{37}$$

where $A(\varphi) = 10^{4\sin(\varphi)-0.3}$.

In Figure 18, we plot J (Eq.37) as a function of φ for three flow rates. The figure shows the rapid increase in J with increase in divergence angle up to $\varphi \approx 14°$, with J constant for $\varphi > 14°$.

Multiple-Row Heat Transfer & Pressure Drop A single serpentine row of screen laminate cannot provide enough surface area. In order to gain more surface area we need to pattern several rows of screen laminate in a series arrangement. Based on the test data for multiple rows, we develop friction factor and Colburn j-factor corrections that account for the decrease in row-by-row performance of a multiple row system. Here we define the overall pressure drop and conductance as ΔP_n and U(tW) as

$$\Delta P_{nrow} = \Delta P_1 \cdot n_{row}^{\,0.35} \qquad 1 \le n_{row} \le 6 \tag{38}$$

$$U(tW)\big|_{nrow} = U(tw)\big|_1 \cdot n_{row}^{\,0.62} \quad 1 \le n_{row} \le 6 \tag{39}$$

From the above equations, it is evident that, with increases in the number of screen-fin rows, the overall conductance increases more rapidly than does the overall pressure drop. So, a larger number of rows is favored with a design that seeks to optimize performance of a heat sink having a pressure drop constraint.

Equations (36)-(39) can be used to design screen-laminate heat sinks. In order to test the accuracy of the design algorithm, we constructed a prototype, measured its pressure drop and heat transfer performance, and compared these results with performance predictions embodied in above equations.

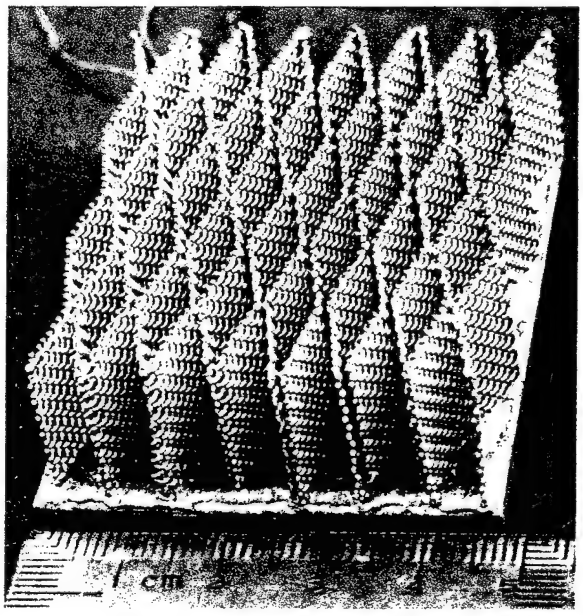

Fig. 19 Prototype Heat Sink

Table 1 Comparisons Between Test Data and Model, $2\theta = 22°$.

		Conductance [watt/°C]					
		4 rows		5 rows		6 rows	
		Model	Test Data	Model	Test Data	Model	Test Data
ΔP[Pa]	24.907	1.15	1.01	1.22	1.105	1.205	1.17
	62.267	1.37	1.255	1.51	1.465	1.555	1.535
	99.628	1.47	1.37	1.66	1.645	1.695	1.745
Standard Error		10.5%		6.3%		2.5%	

The prototype is a simple finned heat sink, 63.5 mm deep, 45.7 mm wide with 23.4 mm high screen-fins (d = 0.483mm, M = 787.402 m^{-1}), as shown as Figure 19. It consists 6 rows of serpentine-pattern screen-fins with divergence angle, 2φ = 22°. We also studied how the row number affects performance by successively cutting the last row from the piece after each experiment so that we measured the performance with 4 rows, 5 rows and 6 rows. In Table 1 we present comparisons between the test data and prototype. The table shows that our model agrees well with our test data. The standard error is less than 11%.

Non-orthogonal Weave Porosity, Specific Surface Area, Effective Thermal Conductivity

Figure 20 summarizes the geometric parameters of the physical model of a diamond-shape plain-weave screen. The figure shows a segment of a plain-weave that comprise a unit cell of the material, together with a section view that illustrates the weave pattern of the wire filaments. Wire filament axes are directed at θ_1 and θ_2 with respect to the presumed heat flux direction (q-direction), so the weave angle is $\theta_1 + \theta_2 = 2\theta$. Serpentine wire filaments have diameter d_1 and d_2 and corresponding mesh numbers M_1 and M_2.If we consider symmetric weaves only, then the mesh number $M=M_1=M_2$, filament diameter $d=d_1=d_2$ and the directions of wire filament axes relative to heat flux direction $\theta_1 = \theta_2 = \theta$.

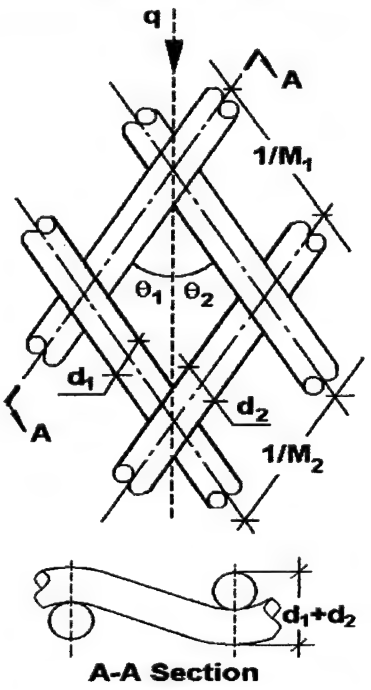

Fig. 20 Diamond-weave unit cell.

Fig.21 shows a typical diamond-shape solder-bonded copper plain-weave screen laminate. The wire filaments have an effective diameter of 0.48mm,

and the mesh number is 6.3cm^{-1} (16 inch^{-1}). The sample has ε = 0.724. (After the bonding, the effective thickness of solder layer over the screen filament ranges from 0.006mm to 0.013mm.)

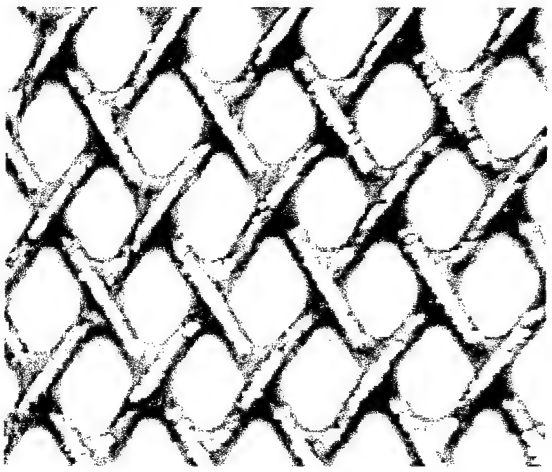

Fig.21 Bonded Diamond-shaped Isotropic Screen Laminates

Consideration of Fig. 20, shows the ratio of the reduced metal fraction of a diamond-weave to an equivalent orthogonal weave can be written as a function of the weave angle (2θ) only; and the same result is obtained with respect to the cf-β-product.

$$\frac{cf_{\pi/2}\cdot(1-\varepsilon_{\pi/2})}{cf_{2\theta}\cdot(1-\varepsilon_{2\theta})}=\frac{cf_{\pi/2}\cdot\beta_{\pi/2}}{cf_{2\theta}\cdot\beta_{2\theta}}=\sin(2\theta) \qquad (40)$$

where the subscript "$\pi/2$" stands for orthogonal, the subscript "2θ" stands for diamond-shape with arbitrary weave angle 2θ. Equation (40) shows that diamond-weaves possess greater metal fraction and specific surface area than orthogonal weaves.

The unit cell shown in Fig.20 is transformed to the layered, rectangular cross section segment shown in the Fig.22. Each rectangular wire filament has thickness $\pi d/4g$ and width gd so that the cross section area of each filament is $\pi d^2/4$. The geometric index, g is a measure of the contact between wire filaments at intersections. We further require that the volume of wire filaments be preserved across the geometric transformation. Then $g=\pi/(4\cdot cf)$.

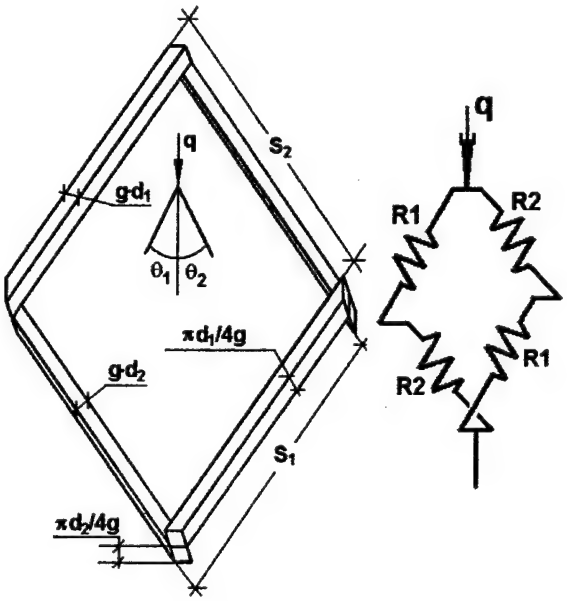

Fig.22 Diamond-weave transformed unit cell and thermal circuit

If we neglect the contribution of the second phase (fluid) to the effective conductivity of the weave, then the in-plane effective thermal conductivity in the q-direction may be determined by considering the thermal circuit for

conduction across the transformed unit cell, which is also shown in Fig. 22. It shows four resistance elements for conduction along the axes of the wire filaments that make up the heat flow path across the transformed unit cell. For a diamond-shaped symmetric screen laminate, the thermal resistance of each filament segment is the same. It is easy to show the total thermal resistance of the unit cell in the q-direction is

$$R_{total} = \frac{-6.25 \cdot 10^{-3} \cdot C}{\pi \cdot k_s \cdot d^2 \cdot M} \tag{41}$$

where C is given in Eq. (22) and k_s is the thermal conductivity of the filament material. The q-direction in-plane effective thermal conductance across the transformed unit cell is,

$$R_{total}^{-1} = k_e \cdot \frac{cf \cdot W \cdot (dx+dy)}{L} \tag{42}$$

where L is the length of unit cell along the q-direction, W is the width of the unit cell perpendicular to the q-direction, and k_e is the in-plane effective thermal conductivity along q-direction. Rearranging Eq. 42 gives

$$cf \cdot Ke = \frac{-80\pi \cdot Md}{\tan(\theta) \cdot C} \tag{43}$$

where $Ke = ke_q / k_s$, is the dimensionless effective thermal conductivity in the q-direction. With the weave angle equal to $\pi/2$, Eq.43 gives the same result for the effective thermal conductivity of the orthogonal weaves (Eq. 26).

We find that for orthogonal isotropic screen laminates, that changing the orientation with respect to the heat flux vectors (i.e. in-plane rotation of the laminates), will not change the in-plane effective conductivity of the structure. So with the same filament diameter and mesh number, the two configurations of orthogonal isotropic screen laminates in the Fig.23 have the same effective in-plane effective thermal conductivity in the q-direction.

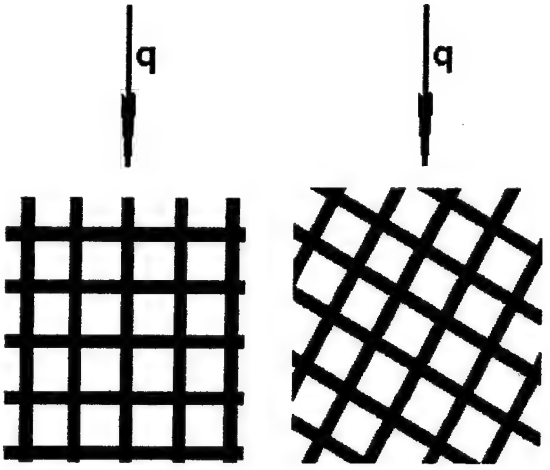

Fig.23 Effect of in-plane rotation on Ke_q of orthogonal plain-weave laminates

The ratio of reduced conductivity of diamond

weaves to orthogonal weaves with the same mesh number and filament diameter can be written as:

$$\frac{cf_{2\theta} \cdot Ke_{2\theta}}{cf_{\pi/2} \cdot Ke_{\pi/2}} = \frac{\sin(2\theta)}{1-\cos(2\theta)} \tag{44}$$

The ratio of conductivity of diamond weaves to orthogonal weaves is plotted in Fig.24 as a function of 2θ. We note that due to the physical limitation of the geometry, there are upper and lower limiting values of the arbitrary weave angle. For the symmetric diamond-shape weave:

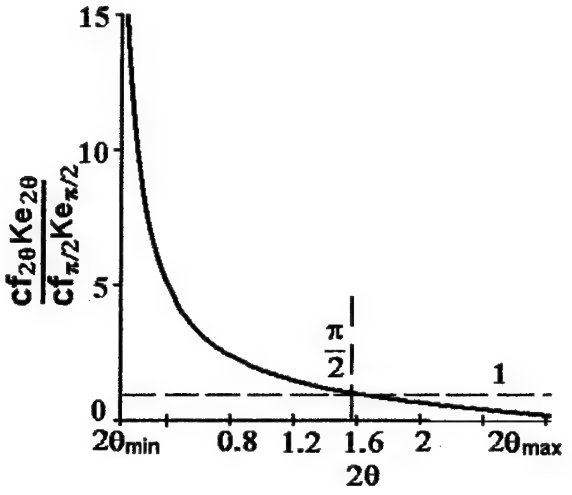

Fig.24 The ratio of conductivity of diamond-weave to orthogonal configuration.

$$2\arcsin(Md/2) \le 2\theta \le 2\arccos(Md/2) \tag{45}$$

Benchmark measurement of the thermal diffusivity of diamond-weave samples (Appendix A) shows that the prediction of the present model is within 8% of all of the measurements.

Exchange Matrix Performance Evaluation

Screen-laminates offer considerable design flexibility. Adjustment of wire diameters and wire pitch allows for control of the structure's porosity, heat transfer surface area-to-volume ratio, and effective thermal conductivity. However, the friction factors and Stanton numbers of the heat exchange matrix are comparable to those of other heat transfer surfaces. The question that must be addressed is: under what conditions does the screen-laminate technology offer superior performance.

In the following, we describe a fixed outer geometry comparison [Webb, 1994] of the performance of a screen-laminate exchange matrix with an exchange matrix consisting of an unconsolidated bed of spherical particles having the same mass (porosity) and face area. The particle bed is selected since both exchange matrices can then be treated as porous media, so that the thin-fin model can be used to predict overall thermal performance. In this way, performance model selection will not influence the ranking of performance.

Table 2 Screen laminate and sphere-bed characteristics

Characteristic	Screen-Laminate	Spheres
External Characteristics	$\varepsilon = 0.4$, $10 \le t/d \le 100$, $10 \le H/d \le 100$ Copper solid phase (k_s= 400 W/mK) Coolant is air @ 300K (Pr = 0.69)	
Internal Geometric	d = 0.5mm , Md=0.556, cf=0.85	d_s = 0.5 mm
Effective Conductivity	88 W/mK, Xu and Wirtz[15]	34 W/mK, Hadley[4]
Specific Surface Area	4800m^{-1}, Eq. (25)	7200 m^{-1}, Kaviany[5]
Pressure Drop	Eq. (32)	Dullien[3]
Matrix Heat Transfer Coefficient	Eq. (34)	Wakao and Kaguei[12]

The thermal performance of a plain-weave screen laminate having porosity (ε = 0.4) is compared with a spherical bed system of the same porosity. This can be achieved with a screen-laminate system having Md=0.556 with cf=0.85. This will result in the two systems having the same mass and external dimensions.

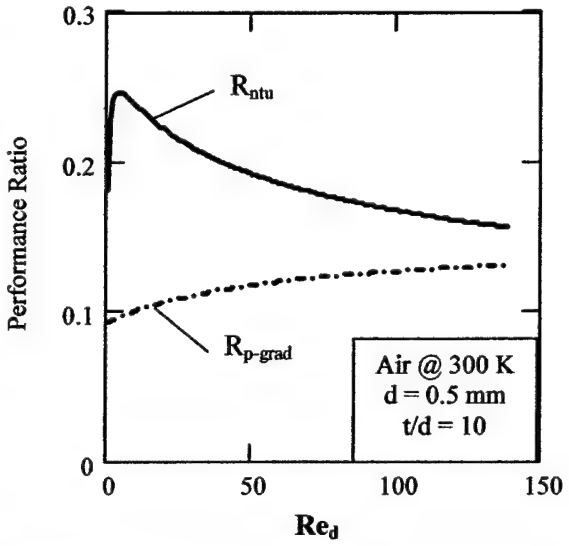

Fig. 25 NTU and pressure-drop performance ratios.

The details of the two systems are summarized in Table 2. Computations are performed with air as coolant. Other, higher Prandtl number fluids produce similar results. External dimensions, thickness and height are varied over a wide range, $10 \le t/d \le 100$, $10 \le H/d \le 100$, while the screen laminate wire diameter and the sphere diameter are held equal to each other, $d = 0.5$ *mm*. Calculations for other diameters give essentially the same results. The table shows that the screen laminate system possesses a higher effective thermal conductivity by a factor of about 2.6, whereas the sphere bed has a higher specific surface area (by a 3:2 ratio).

We define the ntu-ratio and pressure drop performance ratios as follows:

$$R_{ntu} = \frac{ntu(screens)}{ntu(spheres)} \qquad R_{p-grad} = \frac{\Delta P(screens)}{\Delta P(spheres)} \qquad (46a,b)$$

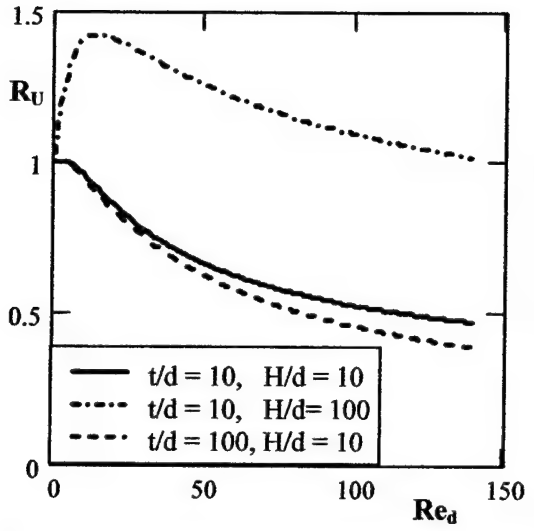

Fig. 26 Screen laminate-to-sphere bed thermal performance ratio, R_U at equal superficial mass velocity

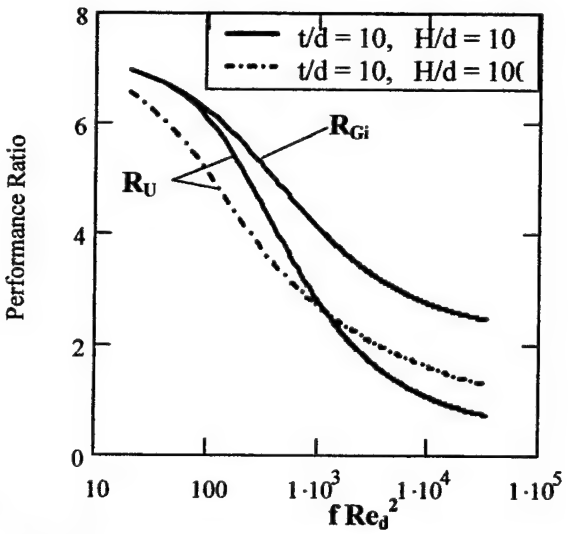

Fig. 27 Screen laminate-to-sphere bed thermal performance ratio, R_U at equal pressure drop

Figure 25 plots these ratios as a function of Reynolds number based on filament size, $Re_d = G_i d / \mu$ for exchange matrices with t/d = 10 (the base line configuration). Re_d reflects variation in superficial mass velocity incident on the exchange matrix. The figure shows that at equal superficial mass velocity, the sphere bed number of transfer units is four to six times greater than that of the screen laminate system. This is due to the higher heat transfer coefficient (h) and specific surface area (β) exhibited by the sphere bed. On the other hand, the pressure drop across the sphere bed is seven to ten times greater than that across the screen laminate.

The results of Fig 25 imply that sphere beds should outperform screen laminate systems at equal coolant flow rates. However, the above analysis does not reflect the 2.6-fold higher effective thermal conductivity of the screen laminate system. In order to assess this component of the problem, we define the "heat duty ratio"

$$R_U = \frac{U(screens)}{U(spheres)} \tag{47}$$

where U, defined by Eq. (1), is calculated from Eq. (8). Figure 26 plots R_U as a function Re_d. The base-line configuration (*t/d = 10, H/d = 10*) shows the sphere bed outperforming the screen-laminate system by up to a factor of two at high coolant flow rates. However, an increase in exchange matrix height (*H/d = 100*) gives rise to a profound change in results. In this case, the screen-laminate system out-performs the sphere bed by up to 40%. This is a reflection of the higher effective thermal conductivity of the screen-laminate system. On the other hand, an

increase in exchange matrix thickness (relative to the base line configuration) gives rise to a slight decrease in performance. It should be noted that while Eqs. (32, 34) include the effect of laminate thickness on mesh heat transfer coefficient, the Wakao and Kaguei Nusselt-number correlation for sphere beds does not.

The situation is further improved (relative to sphere bed thermal performance) if the comparison is done on the basis of equal pressure drop. Figure 27 plots R_U versus the dimensionless pressure drop, fRe_d^2. In this case the base-line configuration (*t/d = 10, H/d = 10*) outperforms the sphere bed by as much as a factor of 7. However, it does so at he expense of vastly increased coolant flow rate, as reflected by a plot of the mass velocity ratio,

$$R_{Gi} = \frac{Gi(screens)}{Gi(spheres)} \tag{48}$$

where the screen laminate flow rate is seen to be as high as 7-times that for the sphere bed. An increase in exchange matrix height gives rise to a reduction in performance advantage at low pressure drop and a slight increase in performance advantage at high pressure drop.

A P4-Format Heat Sink Based on Screen Laminate Technology

The previous analysis indicates that air cooled heat sinks based on screen-laminate technology are promising alturnatives to dense folded-fin heat sinks that are currently used in commercial microprocessor cooling applications. In the following, we describe a novel high-performance heat sink based on *screen-fin* technology. The objective is to design a P4-format air cooled heat sink, having a 3" x 2.5" footprint and 2" height that will have an overall thermal resistance (excluding the base plate spreading resistance) of 0.2 °C/watt at 0.25" H_2O pressure drop of the coolant. This is the unofficial industry benchmark for a longitudinal fin heat sink.

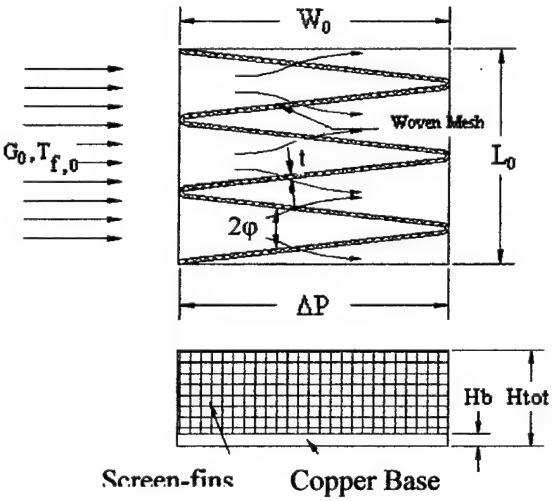

Fig. 28 Schematic of screen-fin heat sink

Screen Laminate Heat Sink Design Concepts Figure 28 shows top and side views of a screen-fin heat sink. The heat sink consists of a base plate (presumed to be in thermal contact with the electronics) and a fin structure. The fin structure consists of a screen-fin oriented perpendicular to the heat sink base, and laid out in a serpentine arrangement so that the divergence/convergence

angle between segments of the screen is 2φ. The external envelope is L_0 wide, W_0 deep, and H_{tot} high. $H=H_{tot} - H_b$ is the fin height. ΔP is the pressure drop across the serpentine screen-fin heat sink. G_0, $T_{f,0}$ denotes the inlet air mass velocity and temperature respectively.

As shown in the figure, the screen-fin is laid out in a serpentine arrangement so that the ambient air with uniform temperature $T_{f,0}$ and flow rate G_0 flows down a converging section, through the screen and then out through a diverging section. This arrangement provides for an increase in heat transfer surface area, and it reduces the superficial mass velocity incident on the screen laminate, thereby effectively controlling coolant pressure drop.

Consider the one-row heat sink segment shown in Fig 29. The heat sink has depth W_0 = 63.5mm, width L_0 =45.72mm, and fin height, H = 38.1mm. At fixed volume flow rate, Q = $G_o(L_oH)/\rho$, variations in θ have two effects on the pressure drop and overall conductance:

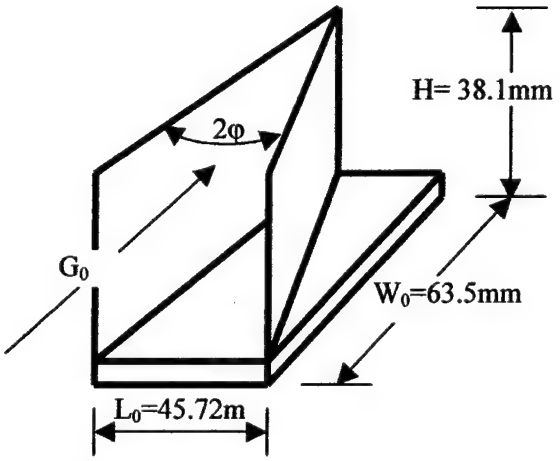

Fig 29 One-row heat sink segment

1. Increasing φ will result in a decrease in heat transfer surface area (As) and friction factor. However the mesh Stanton number will increase as per Eq. (37) and mesh Stanton number will vary with φ.
2. On the other hand, the heat transfer surface area will increase with decreasing φ since more screen-fin segments can be placed on the base plate. However, at fixed flow rate, an increase in surface area will result in a decrease in G_i, resulting in a decrease in Stanton number.

Figure 30 shows the overall effect of variation in φ on overall conductance of the segment when Q = 9.439 liter/sec. The figure shows

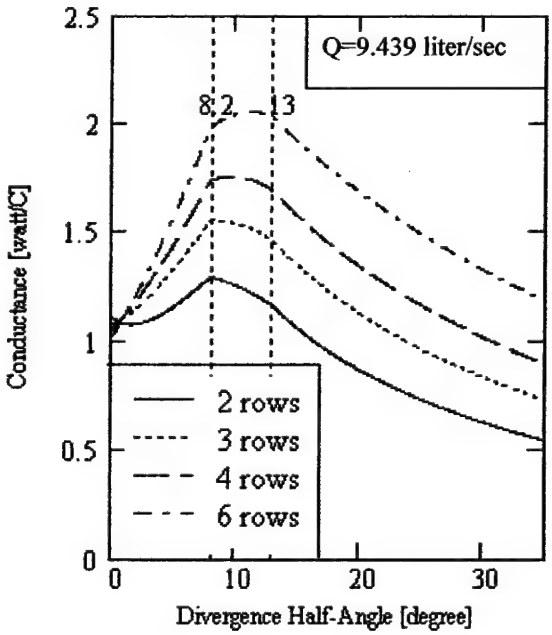

Fig. 30 Effect of Angle of incidence

that $8° < \varphi < 13°$ produces the highest unit surface conductance (depending on the number of screen-fin rows), with lower conductance indicated at higher and lower values of φ. This analysis also shows that the overall pressure drop is minimum when $11° < \varphi < 20°$. Approximately the same result obtains for other flow rates.

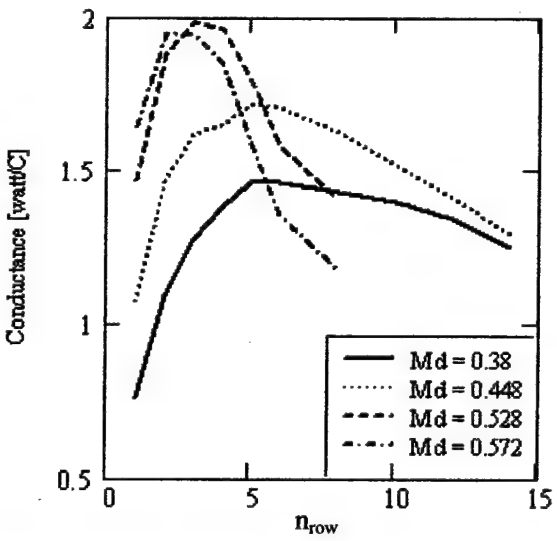

Fig. 31 Effect of Number of Rows, ΔP = 62 Pa.

Figure 31 shows that the conductance of the screen-fin heat sink segment changes with row number with other conditions fixed. At small n_{row}, the surface area increases with the row number; so does the performance of the heat sink. But with further increase in n_{row} the flow rate reduces, leading to a decrease in overall performance. For given Md-product and applied ΔP there will be an optimum value of n_{row}. The figure shows that for the current overall configuration with $\theta = 11°$, $\Delta P = 62$ *Pa (0.25 inch* H_2O), an optimum exists at $n_{row} = 5$, $Md = 0.528$. Other optimums obtain for other configurations.

Table 3 Screen-fin heat sink characteristics. L_o = 63.5mm, W_o = 76.2mm, H = 38.1mm

Parameter	Screen-Fin Heat Sink
Material	Copper Plain-weave
Fin spec	d = 0.56mm (0.022"), M = 9.45 cm^{-1} ($24in^{-1}$)
θ	14°
Thermal Conductivity	72 watt/(m·K)
n_{row}	5
H.T. Surface Area	0.154 m^2
Weight of Fin Structure	193 gram
Coolant flow @ ΔP = 62 Pa	8.0 liter/sec

Optimum Design of Screen Laminate Heat Sink Based on the above discussion, an optimum design does exist for a given size (L_o, W_o, H) and applied pressure drop, ΔP_n. If we consider a heat sink with a 76.2mm x 63.5mm (3" x 2.5" footprint) having 38.1mm (1.5") tall screen–fins and operating at ΔP = 62 Pa (0.25" H_2O), then systematic variation of design parameters results in the optimal design copper heat sink with properties summarized in of Table 3. The fin format of this prototype is as shown in Fig. 19. This heat sink will have an overall conductance of 4.3 watt/°C (thermal resistance = 0.23 °C/watt) when operated at ΔP_n = 62.27 Pa. This is within 14% of the target benchmark, well within the error tolerance that we would place on the analysis.

Assuming a 0.25" thick base plate (typical for this application) the prototype is 0.25" shorter than the target. A conventional heat sink would of necessity be of folded fin design, with a very fine fin pitch. On the other hand, the screen-fin prototype is quite simple in construction. The mass of the fin structure (193 gm) is about the same as would be of an aluminum folded fin design. Furthermore, since the present prototype is all copper, the usual issues that accompany bonding aluminum fins to a copper base plate would not be present. Figure 32 plots the expected performance of the screen-fin prototype.

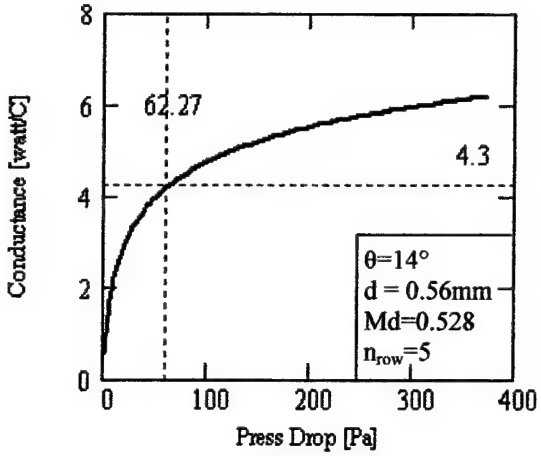

Fig. 32 Optimum design of screen-fin heat sink.

Three-Dimensional Orthogonal Weaves

The following material demonstrates the fabrication methodology of a 3-D, aluminum wire filament, bonded mesh deployed as a heat exchange surface. Models of the porosity, specific surface area and effective thermal conductivity of the mesh is developed. Mesh Stanton number and friction factor correlations for a coolant with Prandtl number equal to 9.5 (chilled water) are reported. Measurements are reported for fabricated test samples of varying thickness. A heat exchanger performance evaluation comparing the 3D woven mesh technology to screen laminate technology is described.

We have found that the weaving/wire bonding process must be carefully controlled to insure that target porosity, specific surface area and effective thermal conductivity are achieved. Effective thermal conductivities are found to be at least two-times larger than achieved in other comparable porous media configurations. Mesh friction factor and Stanton number are comparable to those achieved with other exchanger surface technologies. An exchanger performance evaluation shows that exchangers having superior performance can be configured.

Stacked Weave Geometry

Figure 33 shows a three-dimensional orthogonal stacked-weave that consists of three separate wire filaments of diameters *dx*, *dy* and *dz*, having axes aligned with the *x*, *y* and *z*-axes, respectively. Coolant flow is presumed to be primarily in the *x*-*z* plane. The y-wire filament diameter, *dy* is larger than *dx* and dz so that the effective thermal conductivity in the y-direction, ke_y is larger than ke_x or ke_z. In this way, heat is transferred to the fluid by conduction primarily along the y-filaments; then to the *x*- and *z*-filaments, which act as fins. The wire filaments are bonded at intersections to facilitate conduction. We designate the three-dimensional orthogonal weave shown in Fig. 1 a "stacked weave" since there is no interweaving of wire filaments in any of the three principal planes. This approach allows for a very dense structure.

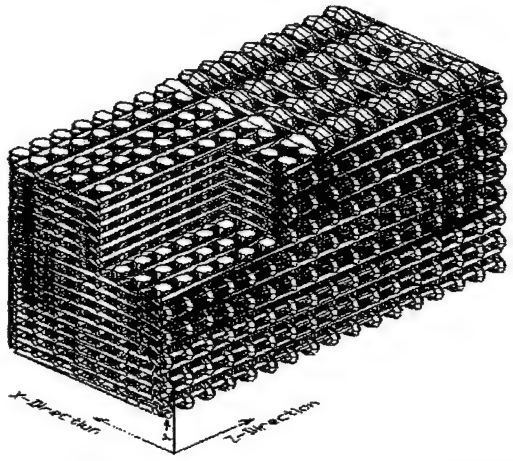

Fig. 33 Three-dimensional orthogonal "stacked" weave.

Mesh Fabrication

Our design objective is to fabricate three 3D stacked weave heat exchange matrixes that are approximately 20mm high x 100mm wide with t = *6.35mm, 9.53mm* and *12.7mm*, respectively.

The mesh is to have *dy = 0.76 mm (0.030")*, *dx = dz = 0.38mm (0.015")*. Analysis in the following section shows that the target metal fraction is (1-ε) = 0.61, and $\beta = 4581m^{-1}$. The target effective thermal conductivity in the y-direction is *84 W/mK*.

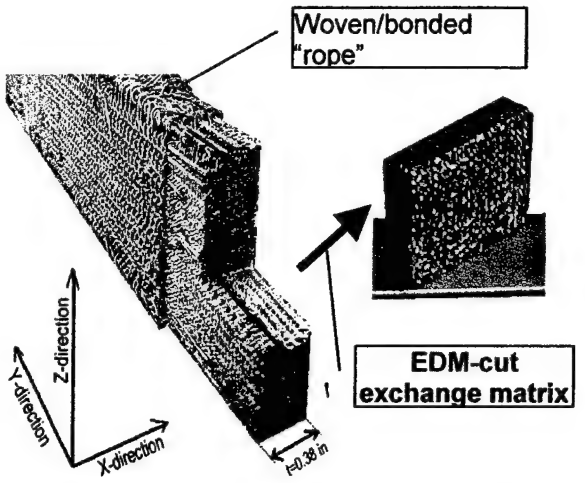

Fig. 34 Three-D woven/bonded mesh fabrication sequence.

The fabrication process involves weaving a wire mesh "rope" of specified wire filament diameters and mesh numbers in the three coordinate directions, braze-bonding the wire filaments at their intersection points, and cutting (via the wire-EDM process) and braze-bonding mesh segments together to form the heat exchange matrix. Figure 34 summarizes the process. Aluminum wire mesh samples (Alloy 1100) were woven on a commercial loom [T.E.A.M. Inc, slatersville RI]. The large diameter wire filaments (*dy*) formed the warp (weave) direction, and dx-wire and dz-wire filaments made up the shut and fill directions. The loom restricted the 3D weave to a product that was approximately 35mm wide x 15mm thick.

The woven "rope" was dip-brazed to bond wire filaments at their intersection points.[1] The process involves impregnating the woven structure with a slurry of al/si eutectic alloy in flux, heating the article to the flux activation temperature, and then immersing the article in a salt bath at 590°C.

Since the dy-wire filaments are in the warp-direction, and the height (y-direction) of the mesh test articles is 20mm, twenty mm long segments of the woven/bonded rope had to be cut, rotated 90°, and then bonded together to form the test article. This was accomplished via wire-EDM.

Table 4 summarizes results of the fabrication process. The table lists target and achieved mesh physical and thermal attributes. Achieved physical dimensions were determined via microscopic

Table 4 Three-dimensional mesh characteristics.

Parameter	Target	Achieved	Δ%
dx, dz, dy [in]	0.015, 0.030	0.0153, 0.031	+1.7
Mx, Mz [1/in]	22.2	20.7	-2.3
My [1/in]	33.3	31.5	-5.5
ε, Porosity	0.39	0.49	+26
β [1/m]	4580(eq 5)	3840 (eq. 2)	-16.2
ke_y [W/m^{2}K]	84 (eq. 13)	75.2	-10.5

inspection of sectioned mesh samples, and the porosity was determined via gravimetric measurements. Details regarding these measurement procedures are documented in [Ruch, 2001]. The achieved values of ke_y is via transient thermal diffusivity measurement [Appendix A].

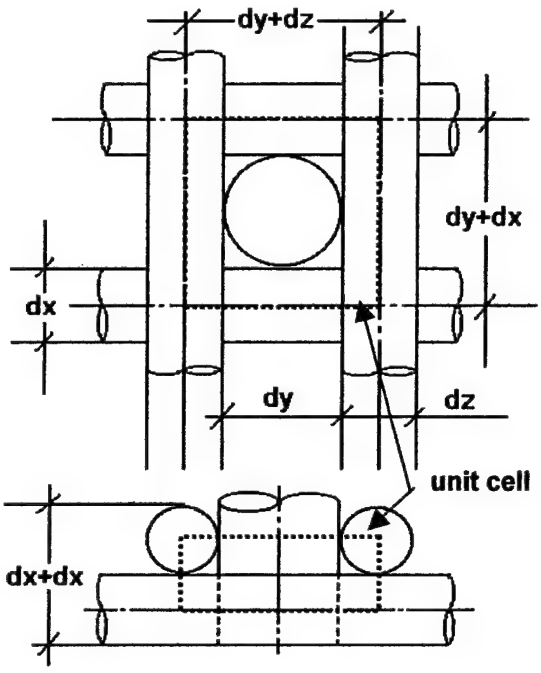

Fig. 35 Three-D stacked weave unit cell.

The Table shows that there was slight wire diameter growth, caused by a combination of wire stretching during the weaving and metal addition due to the brazing process. More significant is the decrease in weave mesh numbers, indicative of a "looser" mesh than targeted. This is due to the inability of the weaver to maintain a "tight" weave, caused by the stiffness of the metal wire filaments and their breakage if too much tension is applied to the wire filaments during the weaving process. The loosening of the mesh results in an increase in porosity, and a decrease in the number of wire intersections that can be brazed together. It was found that about 80% of wire filament intersections are satisfactorily/partly bonded. The remainder are either un-bonded, or the bonds contain faults [Ruch, 2001]. The reduction in metal fraction and wire intersection bonds gives rise to a reduction in heat transfer surface area (β), and effective thermal conductivity (ke_y), and this results in a reduction on performance (Eq. 10).

Three-dimension weave setup is very labor intensive, and it must be carefully controlled since the weaving of aluminum filaments is problematic. Relatively small errors in mesh number result in significant changes in porosity, specific surface area and effective thermal conductivity. As a consequence, this methodology is probably best applied to situations where large volume manufacture is anticipated.

Porosity, Specific Surface Area and Effective Thermal Conductivity

Figure 35 shows a unit cell of the weave of Fig. 1. The wire pitch in each of the coordinate directions are Mx^{-1}, My^{-1} and Mz^{-1} (M is the "mesh number"). Consideration of this unit-cell shows that the porosity (ε) and specific surface area (β) are given by the following expressions:

$$1-\varepsilon=\frac{\pi}{4}\left(dx^2MyMz+dy^2MxMz+dz^2MxMy\right) \tag{49}$$

$$\beta=\pi\left(dxMyMz+dyMxMz+dzMxMy\right) \tag{50}$$

The quantity *(1-ε)* is the volume "metal fraction".

For the current application, we require that wire filaments touch at all possible filament intersections so that filaments can be bonded to facilitate conduction within the mesh. Then

$$Mx=\frac{1}{dy+dz} \qquad My=\frac{1}{dx+dz} \qquad Mz=\frac{1}{dx+dy} \tag{51}$$

Furthermore, let $dx = dz$, and define the filament diameter ratio, $r = dy/dx$. Equations (49) and (50) become

$$1-\varepsilon=\frac{\pi}{4}\left[\frac{1+r+r^2}{(1+r)^2}\right] \tag{52}$$

$$\beta dy=S(1-\varepsilon) \tag{53}$$

where

$$S=4r\frac{1+2r}{1+r+r^2} \tag{54}$$

is the shape factor. Equations (52 - 54) show that once we restrict our attention to bondable 3-D weaves; the βdy-product and the porosity are functions of the filament diameter ratio only.

Figure 36 plots βdy of the 3D stacked weave versus metal fraction for diameter ratio, $0 \le r \le \infty$. The figure shows that bondable 3-D stacked-weaves with $r \ge 1$ can be configured to have metal fraction ranging from 0.589 to $\pi/4$ while $2.36 \le \beta dy \le 2\pi$. Our design objective is to fabricate a 3D stacked weave heat exchange matrix having $r = 2$. The

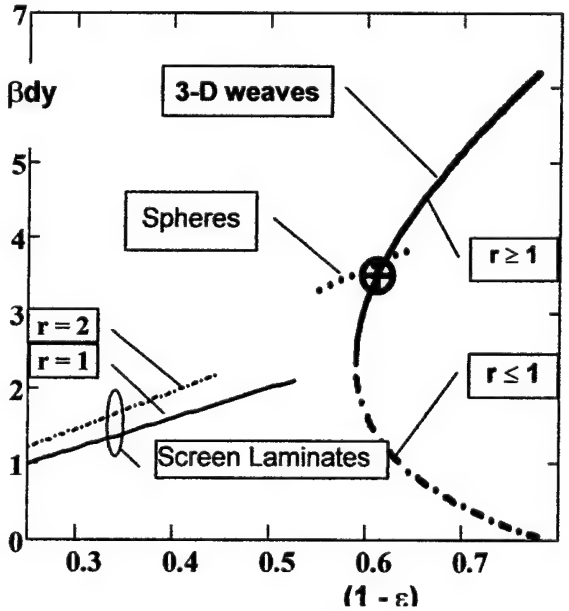

Fig. 36 Specific surface area vs. metal fraction of porous materials.

target metal fraction is then $(1-\varepsilon) = 0.61$, and $\beta = 4581m^{-1}$. The target point, $\{r = 2, (1-\varepsilon) = 0.61, \beta dy = 3.49\}$ is also shown in the in the figure.

Furthermore, the specific surface area formula, Eq. (53) takes the familiar form of other porous media. For example, the shape factor for an unconsolidated bed of spheres is $S = 6$ [Kaviany, 1995] and Xu and Wirtz [2003] have shown that isotropic plain-weave screen-laminates ($dy=dz$, $My=Mz$) have $S = 4$. These functions are shown in the figure. The figure shows that our target design point will have a porosity and specific surface area roughly equivalent to that of an unconsolidated bed of spheres. Larger diameter ratios, r will result in larger achievable specific surface areas.

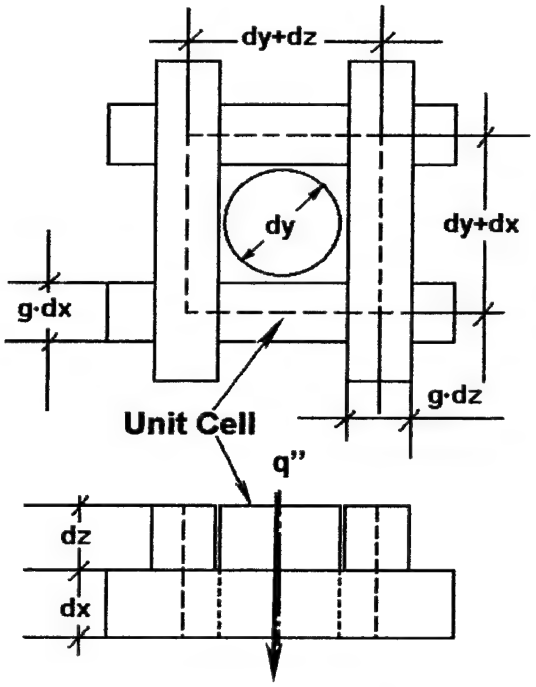

Fig. 37 Transformed unit cell.

Xu and Wirtz [2003] show that isotropic plain-weave laminates can be fabricated to have $0 \le (1-\varepsilon) \le 0.534$. Under these conditions, $0 \le \beta dy \le 2.13$. The figure shows that addition of a third filament to create a 3D orthogonal weave allows for the structuring of a mesh having a larger metal fraction and considerably larger specific surface area.

3D Woven-Mesh Effective Thermal Conductivity. Following Chang [1990], we transform the x- and z-direction wire filaments of the unit cell into rectangular cross section segments shown in Fig. 37. Each rectangular wire filament has thickness $\pi d/4g$ and width gd so that the cross section area of each filament is $\pi d^2/4$. We further require that the volume of the unit cell be preserved across the geometric transformation. Then $g = \pi/4$.

The in-plane effective thermal conductivity in the y-direction may be determined by considering the thermal circuit for conduction in the y-direction across the transformed unit

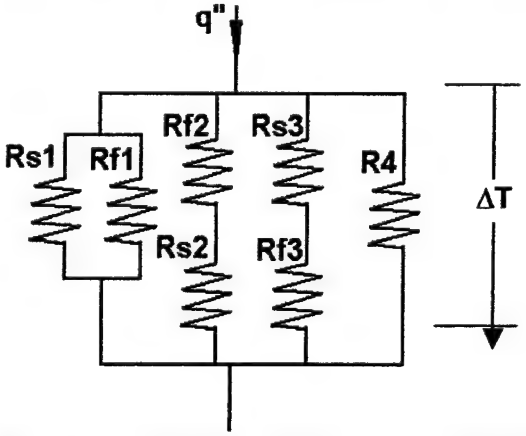

Fig 38 Thermal circuit for y-direction conduction.

cell, shown in Fig. 38. Referring to the transformed unit cell: the parallel path (*Rs1,Rf1*) represents conduction along the axis of the central dy-filament and surrounding fluid; the series paths (*R2 = Rf2+Rs2*) and (*R3 = Rs3+Rf3*) represent conduction across dx- and dz-filaments and fluid regions above and below each filament, respectively; and, *R4* represents conduction across the dx-dz filament intersections.

$$R1 = \frac{4(dx+dy)\cdot dy^{-2}}{\pi\cdot k_s - 4k_m\cdot\left[(1-g)\left(\frac{dx}{dy}+\frac{dz}{dy}\right)+1-\pi+(1-g)^2\left(\frac{dx}{dy}\cdot\frac{dz}{dy}\right)\right]} \tag{55}$$

$$R2 = \frac{dx\cdot k_f + dz\cdot k_s}{k_s\cdot k_f\cdot g\cdot dx\cdot[dz(1-g)+dy]} \tag{56}$$

$$R3 = \frac{dz\cdot k_f + dz\cdot k_s}{k_s\cdot k_f\cdot g\cdot dz\cdot[dx(1-g)+dy]} \tag{57}$$

$$R4 = \frac{dx+dz}{k_s\cdot(g^2\cdot dx\cdot dz)} \tag{58}$$

where k_s and k_f are the thermal conductivity of the solid and "fluid" phases, respectively. If we define the effective thermal conductivity in the y-direction as

$$q = \frac{ke_y(dx+dy)(dz+dy)\Delta T}{dx+dz} \tag{59}$$

then

$$Ke_y = \frac{\pi\cdot r^2(1-k_{fs})+4k_{fs}[r^2+(1-g)^2]+8k_{fs}\cdot r\cdot(1-g)+4g^2}{4(1+r)^2} + \frac{4k_{fs}\cdot g\cdot(r+1-g)}{(k_{fs}+1)(r+1)^2} \tag{60}$$

where $Ke_y = \frac{ke_y}{k_s}$ and $k_{fs} = \frac{k_f}{k_s}$. In most cases the ratio k_{fs} is small; so, if $k_{fs} \approx 0$ the dimensionless effective thermal conductivity becomes a function of diameter ratio, r only,

$$Ke_y\big|_{k_{fs}=0} = \frac{\pi}{4}\left(\frac{r^2+\pi/4}{(r+1)^2}\right) \tag{61}$$

Figure 39 plots $Ke_y(k_{fs}=0)$ vs the metal fraction. Also shown in the figure is the expected dimensionless thermal conductivity for a bed of fused spheres, metal foam and that for a plane weave screen laminate. The figure shows that for r ≥ 1, the dimensionless effective thermal conductivity of the 3-D weave can range from 0.351 up to π/4 while the metal fraction ranges from 0.589 up to π/4. The target design point, *{r = 2, (1-ε) = 0.61}* gives Ke_y = 0.481. This is compared to a fused bed of spheres, which is expected to have Ke_y(spheres) ≈ *0.15*. Furthermore, incorporation of a third wire filament results in a dramatic increase in the effective thermal conductivity relative to that obtained with screen laminate structures.

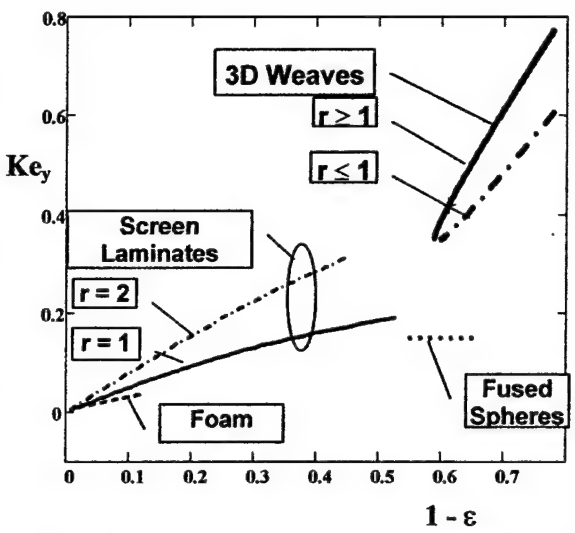

Fig. 39 Effective thermal conductivity of expanded materials.

Heat Transfer, Pressure Drop Correlation

We postulate that the mesh heat transfer coefficient, *h* is functionally related to fluid and flow properties as follows:

$$h = f(\rho, G, \mu, c_f, k_f dy, \beta, t, r, \varepsilon) \tag{62}$$

Dimensional analysis gives

$$St = fn(\mathrm{Re}, \mathrm{Pr}, r, \varepsilon, \frac{dy}{t}) \tag{63}$$

where $\mathrm{Re} = \frac{GD_h}{\mu}$ is the mesh Reynolds number with $D_h = \frac{4\varepsilon}{\beta}$ the mesh hydraulic diameter. In a similar way, we postulate that the pressure drop across the mesh, *ΔP*, is functionally related to fluid and flow properties as follows:

$$\Delta P = fn(\rho, G, \mu, \beta, t, r, \varepsilon) \tag{64}$$

Then dimensional analysis gives

$$f = fn(\mathrm{Re}, r, \varepsilon) \tag{65}$$

where $f = \dfrac{2\rho\Delta P}{G^2 \beta t}$ is the friction factor. It is noted that Eqs. (62) and (64) are the same as Eqs. (28) and (30) for isotropic plain-weave laminates (r = 1). Therefore, we anticipate that Eqs. (63) and (65) will take the same functional form as their correlations or friction factor and Stanton number.

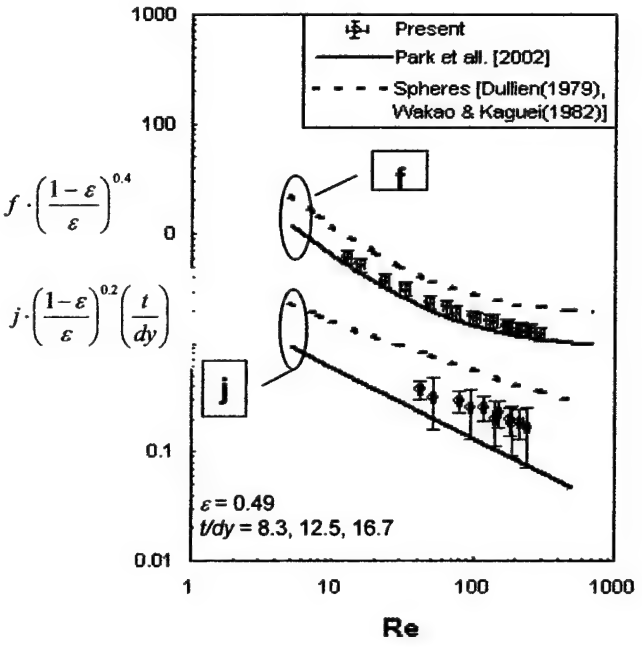

Fig.40 Modified friction factor and Colburn j-factor.

Experiments are performed to measure the pressure drop and porous wall effective conductance. Then, the mesh Stanton number is determined from Eq. (8). The functional forms of Eqs. (63) and (65) are then determined. Pressure drop and heat transfer experiments use the same channel flow apparatus and data reduction procedures as described in Appendix B.

Figure 40 compares measured friction factor,

$$f = \frac{\Delta P}{\frac{1}{2}\frac{G^2}{\rho}\beta t} \tag{66}$$

and j-factor,

$$j = St \cdot \mathrm{Pr}^{2/3} \tag{67}$$

for the present 3D stacked weave (ε = 0.49, t = 6.35mm, 9.53mm and 12.7mm) with correlations for spheres (ε = 0.39) and isotropic plain-weave screen-laminates. Ninety-five percent (95%) confidence level error bars are shown on the figure. The present data lays intermediate to these two other configurations. The friction factor is correlated as

$$f = \left[1.078 + \frac{64}{\mathrm{Re}}\right]\left(\frac{1-\varepsilon}{\varepsilon}\right)^{-0.4} \tag{68}$$

The first term of Eq. (68) represents the inertial contribution to the pressure drop; and, the second term represents the viscous contribution. Since the present experiments consider only a single

Table 5 Three-dimensional orthogonal mesh characteristics.

Characteristic	3D Weave	Screen-Laminate
External Characteristics	$t = 3.175$mm, $2H = 2t, 4t, 8t$ Aluminum, Alloy 1100 Coolant is Air @ 300K ($Pr = 0.69$)	
Internal Geometric	$dy = 0.41$ mm r = 2, $\varepsilon = 0.385$ "stacked"	$Md = 0.577$ $\varepsilon = 0.466$ $dy = dz = 0.35$ mm "in-line" laminate
β [m^{-1}]	8589,Eq. (5)	6073, Eq. (25)
ke_y [W/mK]	84, Eq. (13)	44 W/mK, Eq. (26)
ΔP [Pa]	Eq. (24)	Eq. (32)
h [W/m^2K]	Eq. (25)	Eq. (34)

mesh porosity, we have used Part et al's [2002] term for the second factor in Eq. (68). Equation (68) reproduces the data that generated it with a standard error of 4.4%. In a similar manor, the j-factor is correlated with a power-law

$$j = 1.89\,\mathrm{Re}^{-0.44}\left(\frac{1-\varepsilon}{\varepsilon}\right)^{-0.2}\left(\frac{dy}{t}\right) \tag{69}$$

Equation (69) reproduces the data that generated it with a standard error of 10.7%.

Exchange Matrix Performance Evaluation

Three-dimensional stacked weaves offer considerable design flexibility. Adjustment of the wire diameter ratio, r allows for control of the structure's porosity, heat transfer surface area to volume ratio, and effective thermal conductivity. However, the friction factors and Stanton numbers of the heat exchange matrix are comparable to those of other heat transfer surfaces. The question that must be addressed is: under what conditions does the 3D-weave technology offer superior performance.

Recognizing that we have shown that screen-laminates can generally be configured to out-perform fused particle systems, in the following we describe a fixed outer geometry comparison of the performance of a 3D-weave exchange matrix with a screen-laminate exchange matrix of the same volume and face area. The two systems are deployed as in a single-fluid parallel-plate heat exchanger such as a cold-plate or flow-through module.

Table 5 summarizes the characteristics of the two systems. Both exchange matrices are made of aluminum (alloy 1100). They have the same thickness, face area and plate-to-plate spacing (three spacing are considered). The coolant is air. Consideration of higher Prandtl number fluids produces similar results. The 3D weave is made up of 0.41mm/0.20mm (16mil/8mil) wire ($r = 2$)

resulting in an exchange matrix with a porosity of 0.385, specific surface area of 8589 m^{-1} and effective thermal conductivity of 84 W/mK.

The tightest weave achievable with an isotropic plain-weave has the product $Md = 0.577$. This results in a porosity of 0.466. A mesh number equivalent to the 3d weave has $M = 16.4$ cm^{-1}. Then, the wire diameter must be 0.35mm (0.014 in). With no interleaving of adjacent screen layers, the specific surface area becomes 6073 m^{-1}, and the effective thermal conductivity is 44 W/mK, roughly half the value achieved with the 3D weave.

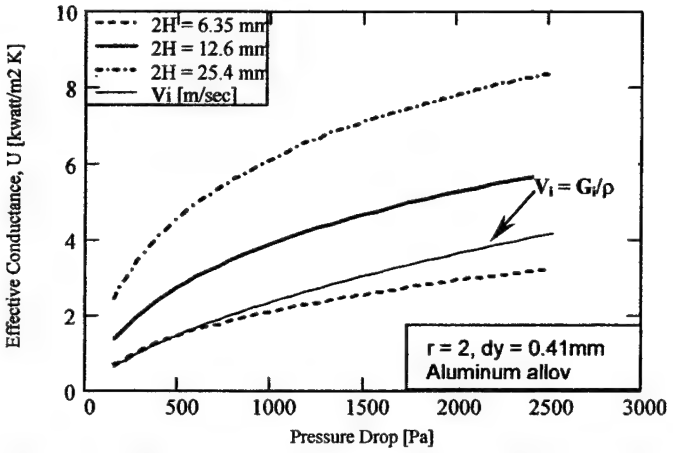

Fig. 41 Effective conductance and superficial coolant velocity of 3D stacked weave. Coolant is air at 300K.

Figure 41 plots the effective surface conductance of the 3D stacked weave as a function pressure drop. Results for three plate-to-plate spacings are shown. Also shown in the figure is the superficial velocity, V_i, as a function of applied pressure drop. At ΔP = 1250 Pa (5 in H_2O), the conductance exceeds 6500 W/m^2K, a value normally associated with liquid-flow turbulent convection or phase-change heat transfer. At this pressure drop, the superficial coolant velocity is approximately 2.7 m/sec.

We define the pressure drop ratio and "heat duty" ratio as

$$R_{\Delta P} = \frac{\Delta P(3D \cdot weave)}{\Delta P(screen \cdot la\,min\,ate)} \qquad (26a)$$

$$R_q = \frac{U(3D \cdot weave)}{U(screen \cdot la\,min\,ate)} \qquad (26b)$$

Figure 42 plots the pressure drop ratio and heat duty ratio as a function of superficial coolant velocity, comparing the 3D-weave to the screen laminate. In every case, the screen laminate pressure drop is significantly lower than that of the 3D weave. However, the

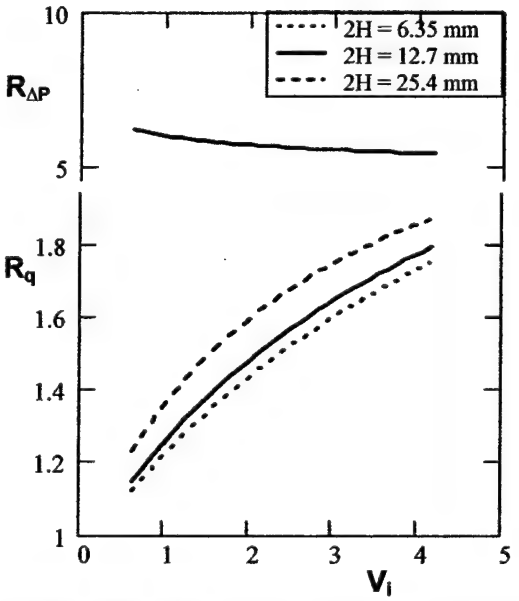

Fig.42 PEC 3D stacked weave vs isotropic plain-weave screen-laminate.

corresponding heat duty ratios are greater than one, indicating that the 3D weave out performs the screen laminate system by about 50%. Figure 42 shows that the heat duty ratio increases with increasing superficial velocity. This is a consequence of the 3D-weave having a higher specific surface area and mesh heat transfer coefficient. The figure also shows that the heat duty ratio also increases with increasing array height. This is a consequence of the significantly higher effective thermal conductivity achieved with the 3D-weave.

Conclusions

A mathematical model of the thermal performance of a woven mesh, deployed as a heat exchange surface, is developed. Woven meshes are modeled as porous media. Since the fluid flow path length through the porous wall is short (by design) and flow rates are relatively high, a two-energy equation model is developed. The present model shows that the effective conductance of a thin, porous heat exchange matrix is proportional to the square root of the product of the specific surface area, effective thermal conductivity and mesh heat transfer coefficient. Furthermore, we propose that mesh heat exchange matrices be laid out in a serpentine pattern, similar to the construction of a conventional automotive air filter. This configuration maximizes heat transfer surface area while it minimizes coolant pressure drop (due to the reduced superficial mass velocity). Analysis of a screen-fin heat sink indicates that the optimal convergence/divergence angle of the serpentine layout is $\approx 20° - 30°$.

Screen Laminate Technology Screen laminates are simple to fabricate structures. They can be constructed to have a wide range of porosity, heat transfer surface area and effective thermal conductivity. Isotropic orthogonal-weave laminations can be configured to have metal fraction $(1-\varepsilon)$ and specific surface area ranging up to $0.534cf^{-1}$ and 2.13 $(cf\,d)^{-1}$, respectively. The in-plane effective thermal conductivity can be as much as 6- times greater than the cross-plane effective thermal conductivity, and the in-plane effective thermal conductivity can range to 19.2% of the filament material value (a thirty to fifty percent improvement over other porous materials). Diamond weaves (and anisotropic weaves) can be configured to have proportionately higher material properties, with the in-plane effective thermal conductivity ranging to 78.5% of the filament material values.

Dimensional analysis is used to establish the definitions of the dimensionless groups that characterize the pressure drop and mesh heat transfer coefficient. Experiments with air and water have been used to establish correlations for the friction factor and mesh Stanton number. Screen laminates are found to exhibit orthogonal flow pressure drop and mesh heat transfer coefficients comparable to other porous media. Experiments with non-orthogonal flow (superficial flow incidence angle = φ) show that the friction factor increases as $\varphi \rightarrow 0$; and, the mesh heat transfer coefficient increases as $\varphi \rightarrow 20°$.

A performance comparison shows that screen–laminate systems can generally be configured to offer thermal and pressure drop performance superior to unconsolidated packed bed matrices. This is particularly true for exchange matrix configurations that exploit the higher effective

thermal conductivity achievable with screen-laminate systems. A design exercise of a screen-fin heat sink for a P4 microprocessor cooling application shows that a simple device can be configured, which rivals the performance of a dense-fin (expensive) unit that is the unofficial industry benchmark.

Stacked Weave Technology Three-dimensional stacked weaves are relatively dense structures, with the βdy-product and porosity functions of the wire diameter ratio only. Metal fractions can range from 0.589 up to 0.785; and, the βdy-product can range up to 2π. Metallic weaves can be structured to have effective thermal conductivity that is two, or more times greater than what can be achieved with other porous media, with y-direction effective thermal conductivity approaching 78% of the filament material value. Mesh heat transfer coefficients and friction factors are comparable to those achieved with other expanded materials. However, high β-values, coupled with high effective thermal conductivity result in exchange matrices that out-perform other exchange matrix configurations in applications where coolant pressure drop is not a critical constraint.

Three-dimension weave setup is very labor intensive, and and it must be carefully controlled since the weaving of aluminum filaments is problematic. Relatively small errors in mesh number result in significant changes in porosity, specific surface area and effective thermal conductivity. As a consequence, this methodology is probably best applied to situations where large volume manufacture is anticipated.

Research Personnel

- R.A. Wirtz (P.I.) University Foundation Professor of Mechanical Engineering, University of Nevada, Reno NV
- Mr. Dan Ruch (MS, completed 8/01) currently Alternative Energy Assoc, Germany
- Jay Ji-Wook Park (MS, completed 12/01) currently Ebara International Corp, Sparks, NV
- Mr. Richard Jun Xu (MS, completed 12/01) currently PhD program, Mechanical Engineering, Perdue University
- Mr. Chen Li (MS, completed 12/02) currently Ph.D program, Mechanical Engineering, RPI

Publications/Thesis

Publications:

Park, J-W, Ruch, D and **Wirtz, R.A.** (2002) "Thermal/Fluid Characteristics Of Isotropic Plain-Weave Screen Laminates As Heat Exchange Surfaces," AIAA Paper 2002-0208, AIAA Aerospace Sciences Meeting, Reno, NV, January 2002.

Xu, J. and **Wirtz, R. A.**, (2002) "In-Plane Effective Thermal Conductivity of Plain-Weave Screen Laminates," *Thermal Challenges in Next Generation Electronic Systems,* Millpress, Rotterdam; also, IEEE J. Components and Packaging Technology, Vol. 25, pp 615 – 620, 2003.

Wirtz, R. A., Jun Xu, Park, Ji-Wook and Ruch D. (2002) "Thermal/Fluid Characteristics Of 3_D Woven Mesh Structures As Heat Exchanger Surfaces," paper no. 1372, Itherm 2002, San Diego, May 2002; to appear, **IEEE J. Components and Packaging Technology**.

Wirtz R.A., Chen Li, Ji-Wook Park and Jun Xu (2002) "High Performance Woven Mesh Heat Exchangers," *Eleventh AIAA/MDA Technology Conference and Exhibit, Monterey CA, July 29 – Aug 2.*

Chen Li and **R.A. Wirtz** (2003) "Development of a High Performance Heat Sink Based on Screen-Fin Technology" Proc. Semiconductor Thermal Measurement and Management Symposium, IEEE #03CH37437, pp 53 - 60; pending **IEEE J. Components and Packaging Technology**.

Jun Xu and **R.A. Wirtz** (2003) "In-Plane Effective Thermal Conductivity of Plain-Weave Screen Laminates with Arbitrary Weave Parameters, Paper TED-AJ03-417, ASME/JSME Thermal Engineering Conference, Hawaii, March 2003; pending **IEEE J. Components and Packaging Technology**.

R.A. Wirtz and Ji-Wook Park (2003) "Thermal/Fluid Characteristics Of Screen Laminate Heat Exchange Matrices" pending, **AIAA Journal of Thermophysics and Heat Transfer**

Thesis:

Ji-Wook Park (2001) "Thermal/fluid characteristics of Isotropic plain-weave screen laminates as heat exchange surfaces", M.S. Thesis, Mechanical Engineering Department/MS 312, University of Nevada, Reno, NV 89557.

D. Ruch (2001) "Thermal/Fluid Characteristics Of 3-D Woven Mesh Structures As Heat Exchanger Surfaces", MS Thesis, M. E. Dept, Univ. Nevada, Reno NV 89557

Jun Xu (2001) "Effective Thermal Conductivity of Screen Laminate Composites", MS Thesis, M. E. Dept., Univ. Nevada, Reno, NV 89557

Chen Li (2002) "Development of a High Performance Heat Sink Pased on Serpentine Woven Mesh Technology", MS Thesis, M. E. Dept., Univ. Nevada, Reno, NV 89557

Acknowledgement/Disclaimer

The Missile Defense Agency through the Air Force Office of Scientific Research, USAF, sponsors this work under contract number F49620-99-0286. The views and conclusions contained herein are those of the authors and should not be interpreted as necessarily representing the official policies or endorsements, either expressed or implied of the Missile Defense Agency, the Air force Office of Scientific Research, or the U.S. Government.

References

1. Ashby, M., Evans, A., Fleck, N., Gibson, L., Hutchinson, J. & Wadley, H. 2000. Metal Foams, A Design Guide. Butterworth Heinemann.
2. Armour, J. C. and Cannon, J. N., "Fluid Flow Through Woven Screens", *AIChE J.*, Vol. 14, 1968, pp. 415-420.
3. Calmidi, V.V. and Mahajan, R.L. "The Effective Thermal Conductivity of High Porosity Fibrous Metal Foams", *J Heat Transfer*, Vol. 121, pp. 466 – 471, 1999
4. Chang, Woo Soon. 1990. "Porosity and Effective Thermal Conductivity of Wire Screens", *Journal of Heat Transfer, Vol. 112.*
5. Coulson, J.M. and J.F. Richardson, *Chemical Engineering, 4-th ed*, Vol. 2, Pergamon Press, Oxford, 1991
6. Dullien, F. A. L., *Porous Media: Fluid Transport and Pore Structure*, Academic Press, 1979.
7. Hadley, G. R., "Thermal Conductivity Of Packed Metal Powders", *Int. J. Heat Mass Transfer*, Vol. 29, 1986, pp. 909-920.
8. Kaviany, M., *Principles of Heat Transfer in Porous Media*, 2nd ed., Springer, 1995.
9. Kays, W. M. and Crawford, M. E., *Convective Heat and Mass Transfer*, 3rd edn., McGraw Hill, 1993.
10. Kays, W. M. and London, A. L., *Compact Heat Exchangers*, 3rd edn., McGraw-Hill, 1984.
11. Koh, J. C. Y. and Fortini, A., "Prediction Of Thermal Conductivity And Electrical Resistivity Of Porous Metallic Materials", *Int. J. Heat Mass Transfer*, Vol. 16, 1973, pp. 2013-2021.
12. Luo, S.Y. & Mitra, A. 1999. Finite Elastic Behavior of Flexible Fabric Composite Under Biaxial Loading. *Journal of Applied Mechanics, Vol. 66, pp 631-638.*
13. Miyabe, H., Takahashi, S., and Hamaguchi, K., "An Approach To The Design Of Stirling Engine Regenerator Matrix Using Packs Of Wire Gauzes", *Proc. 17th IECEC*, 1982, pp. 1839-1844.
14. *Park, Ji-Wook, "Thermal/Fluid Characteristics Of Isotropic Plain-Weave Screen Laminates As Heat Exchange Surfaces", M.S. Thesis, 2001, Mechanical Engineering Department/MS 312, University of Nevada, Reno, NV 89557.*
15. Ruch, D."Thermal/Fluid Characteristics Of 3-D Woven Mesh Structures As Heat Exchanger Surfaces", MS Thesis, M. E. Dept, Univ. Nevada, Reno NV 89557, 2001
16. Tong, L. S. and London, A. L., "Heat-Transfer And Flow-Friction Characteristics Of Woven-Screen And Crossed-Rod Matrixes", *Trans. ASME*, 1957, pp. 1558-1570.
17. Wakao, N. and Kaguei, S., *Heat and Mass Transfer in Packed Beds*, Gordon and Breach Science Pub., 1982.
18. Webb, R. L., *Principles of Enhanced Heat Transfer*, John Wiley and Sons, 1994.

19. Wirtz, R. A., "A Semi-Empirical Model For Porous Media Heat Exchanger Design", *Proc. 32nd National Heat Transfer Conference*, ASME HTD-Vol. 349, 1997, pp. 155-162.

20. R. A. Wirtz, Jun Xu, Ji-Wook Park and Dan Ruch, "Thermal/Fluid Characteristics of 3D Woven Mesh Structures as Heat Exchanger Surfaces," Paper #1372, Eighth Intersociety Conference on Thermal and Thermomechanical Phenomena in Electronic Systems.

21. J. Xu "Effective Thermal Conductivity of Screen Laminate Composites", MS Thesis, M. E. Dept., Univ. Nevada, Reno, NV 89557, 2001

22. Xu, J. and Wirtz, R. A., "In-Plane Effective Thermal Conductivity of Plain-Weave Screen Laminates", *IEEE Trans, Components and Packaging Technology, Vol. 25, pp. 615 - 620*, 2003.

Appendix A: Measurement of *ke*

Consider a uniform cross section, long and slender test article with well-insulated periphery, as shown in Fig. A1. The test article is initially at a uniform temperature, T_i when a time-varying heat flux is applied to one end. We measure the temperature response at three locations, as shown in the figure. Assume constant thermophysical properties and one-dimensional transient conduction in the domain between points 1 and 3. The temperature response at point 2 will be given as

$$T2(\tau) = fct[T1(\tau), T3(\tau), \Delta y_1, \Delta y_2, \alpha] \qquad (18)$$

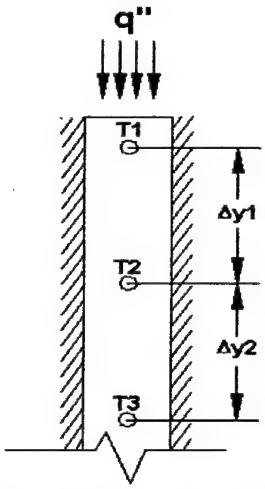

Fig. A1 Test Configuration.

The temperature response at point 1 describes the heat input to the test domain; that at point 3 describes the heat outflow from the test domain. Then, the temperature response at point 2 can be used to determine the thermal diffusivity, α, [7].

The test rig consists of a radiant heat source and shutter mechanism, and well-insulated screen laminate test articles that are approximately 200mm long, as shown in Fig A2. Temperatures at points 1, 2 and 3 are sensed with 0.25mm diameter Type T thermocouples that are soldered to the test article. Measurement points are located with an accuracy of ±0.1mm. Temperatures are recorded at a rate of 10 – 20 samples per second, with an accuracy of approximately ±0.2°C.

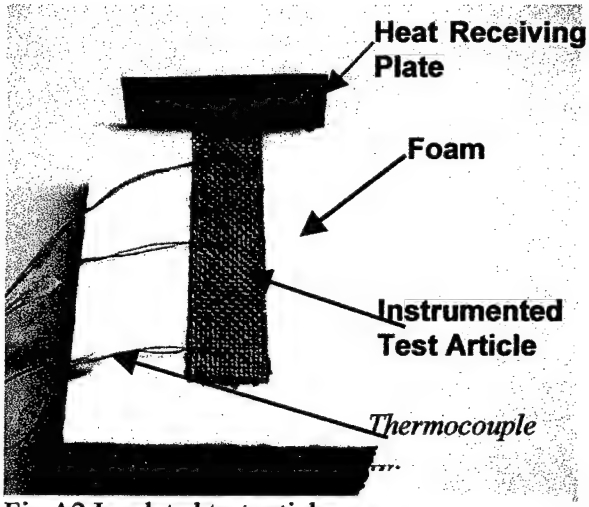

Fig A2 Insulated test articles.

Measurement Calibration Three bar-shaped oxygen-free copper test articles (Alloy C10100, $\alpha = 11.1x10^{-5}m^2/s$) were tested. Each test was repeated six times. The mean measured thermal diffusivity for each of the test articles was $11.76x10^{-5}m^2/s$, $11.62x10^{-5}m^2/s$ and $11.72x10^{-5}m^2/s$, giving an overall

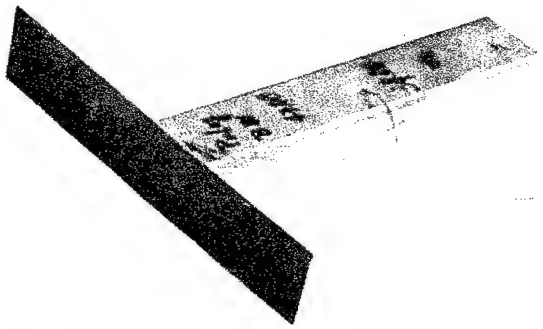
Fig A3 Copper calibration test articles.

average value of $11.7x10^{-5}m^2/s$. The 95% confidence interval for all 18 measurements (2σ about mean values) is $0.7x10^{-5}m^2/s$ and the implied offset error, based on the handbook value of thermal diffusivity of alloy C10100, is +5.2%.

Screen Laminates Test Articles Isotropic, orthogonal weave and diamond weave plain-weave copper screens are stacked and bonded together (using 95/5 Sn/Pb solder) to form the screen laminates. Various screen laminate samples were fabricated with this method: the mesh numbers range from $6.3cm^{-1}$ $(16inch^{-1})$ to $15.75cm^{-1}$ $(40inch^{-1})$, the bare copper wire filament diameter ranges from *0.28mm(11/100 inch)* to *0.46mm(18/1000inch)*, and the number of layers ranges from 3 to 10. Measured compression factors range from 0.70 to 1.00. Figure A4 shows a typical experimental result where Tc(t;α) is the calculated temperature response of point 2 with $\alpha e = 5.35x10^{-5}$ m^2/sec.

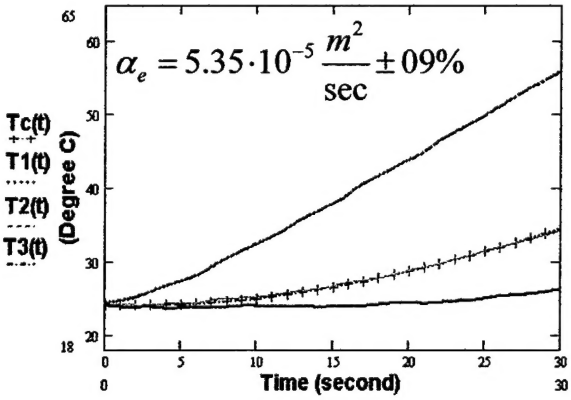

Fig A4 Typical test result.

In the calculation of ke, the effective density/specific heat product of the screen laminate, ρc is calculated based on the measured weight ratios of copper and solder material in the composites. The copper wire properties are: $\rho = 8940$ kg/m^3, c = 393.5 J/(kg·K), $k_s = 400$ W/(mK). The Sn-Pb solder material's properties are: $\rho = 7317$kg/m^3, c = 230.0J(/kg·K), $k_s = 56$ W/(mK). As different specimens have different weight ratios of copper and solder material, so the calculated effective densities for the laminates range from 8694kg/m^3 to 8796kg/m^3, the specific heats range from 369.1J/kg·K to 379.0J/kg·K and, the thermal conductivity range from 349.7 W/mK to 371.1 W/mK. The thermal conductivity of air (0.0278W/(m·K)) at temperature of 323K, is used.

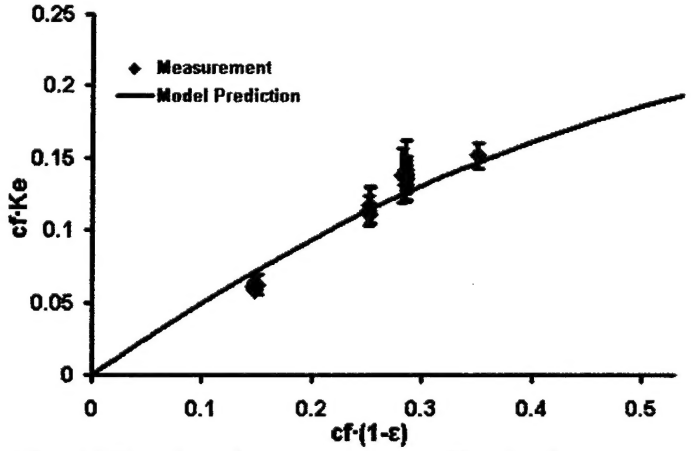

Fig. A5 Benchmark measurements of ke_y in air.

Test results. The average test result of dimensionless reduced in-plane effective conductivity for orthogonal weave specimens is

shown with 2σ error bars in Figure A5. Each data point shown represents six or more test runs of the same sample. The model prediction for the isotropic plain-weave screen laminate saturated with air is also shown in the figure. It shows that the prediction of the present model is within 10% of all of the measurements. With consideration of the non-uniform solder layer's thickness on the filaments, and non-uniform properties of the high porosity screens, the prediction of the present model is quite accurate.

Appendix B: Heat Transfer/Pressure Drop Measurements

Pressure drop and heat transfer experiments are done in two different channel-flow apparatus. A schematic of the test section for either apparatus is shown in Figure B1. The figure shows an edge view of a screen laminate, of thickness t, located in a parallel-plate channel, which is approximately 18 mm high x 100 mm wide. A fluid, at mass velocity (G_i) and temperature ($T_{f,i}$) passes through the test article. The test article is heated from the side. Thermocouples measure the inlet temperature and base temperature. Coolant pressure drop is measured with an electronic manometer having ±4% accuracy.

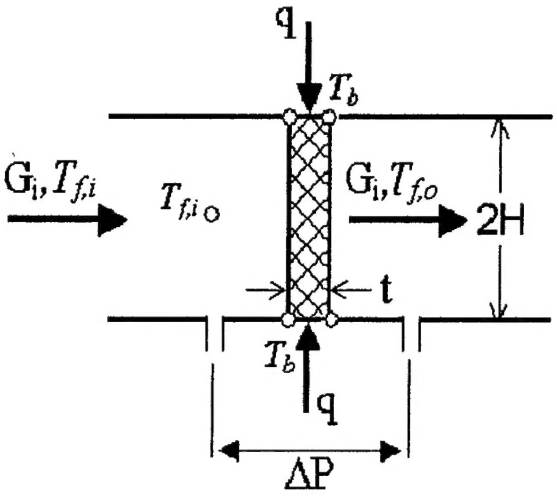

Fig. B1 Edge view of mesh exchange matrix test section.

Air flow experiments The channel is of open-loop, induced-draft design. Laboratory air passes through a honeycomb flow straightener; the test article; a second flow straightener; a plenum chamber and suitably long pipe to a laminar flow element, which measures the volumetric flow rate; and, then to a variable speed exhauster. The laminar flow element has ±3% accuracy.

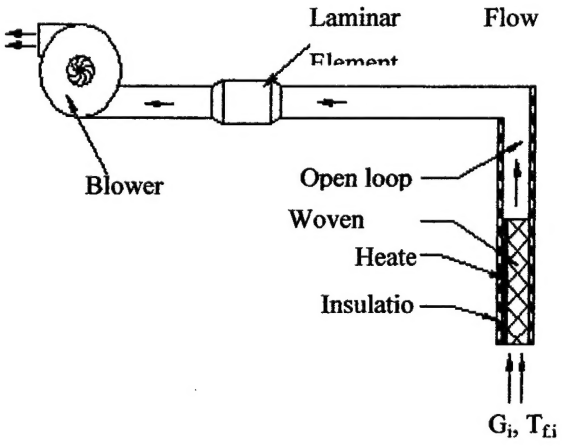

Fig. B2 Air-flow test rig.

A thin film heater applies power to the bottom (one side) of the test article. Thermocouples are used to monitor the base temperature of the test article and inlet air temperature. We estimate that heat losses out of the bottom of the test rig are less than 2% of the input power (q), temperature measurements are accurate to ±0.05°C, and q is measured to ±4%.

Liquid flow experiments. Experiments are conducted in a closed loop chilled water flow apparatus shown schematically in Fig. B3. The test rig consists of a pump/fluid reservoir, heat

copper screen with d = 0.48 mm (0.019"), M = 7.9 cm^{-1} ($20in^{-1}$) with $\varepsilon = 0.677$. A total of 18 samples were tested where the flow rate was varied over the following range: $1.76 \leq Re \leq 300$. All experiments were performed at least twice (on different days), to check the repeatability of the data. A Monte Carlo error propagation simulation indicates the following 95%-confidence level tolerance on computed results: Re less than ±5%; f less than ± 15%; St less than ±10%.